CHEMISTRY OF MATERIALS

Open Access

pubs.acs.org/cm

Article

Fundamental Thermodynamic, Kinetic, and Mechanical Properties of Lithium and Its Alloys

Sesha Sai Behara, Jeremiah Thomas, and Anton Van der Ven*

Cite This: *Chem. Mater.* 2024, 36, 7370−7387

Read Online

ACCESS | Metrics & More | Article Recommendations | Supporting Information

ABSTRACT: Lithium alloying reactions are beneficial in promoting uniform plating and stripping of lithium metal in all-solid-state batteries. First-principles calculations are performed to predict thermodynamic, kinetic, and mechanical properties of lithium and several important Li−M alloys (M = Mg, Ag, Zn, Al, Ga, In, Sn, Sb, and Bi). While the Li−Mg binary system forms a solid solution, most other lithium−metal alloys prefer stoichiometric intermetallic compounds with common local motifs that enable fast Li diffusion. Lithium and Li-rich alloys exhibit an unusually flat energy landscape along paths that connect BCC to close-packed structures like FCC and HCP, with important implications for mechanical properties. Very low migration barriers for Li diffusion that rival those of superion conductors are predicted, both in pure Li and in Li−M intermetallics. However, vacancy concentration, which is crucial for substitutional diffusion, is predicted to be low in metallic Li and most Li−M intermetallics. Compounds such as B32 LiAl and LiGa as well as $D0_3$ Li_3Sb and Li_3Bi exhibit structural vacancies at higher ends of their voltage windows, which together with low migration barriers leads to exceptionally high Li mobilities. In the Li−Mg solid solution, the addition of Mg is found to decrease the vacancy tracer diffusion coefficient by an order of magnitude.

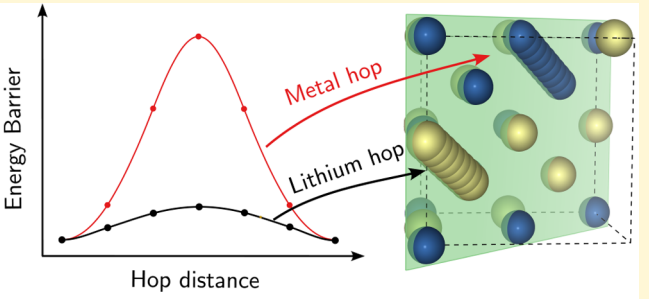

1. INTRODUCTION

All-solid-state batteries promise significant increases in the energy densities of Li-ion batteries, as they will enable the replacement of graphite with lithium metal as the anode.[1] Anode-free solid-state batteries are especially attractive since they are less challenging to manufacture. The Li that is to be shuttled between the cathode and the anode of an anode-free battery is introduced as part of the fully lithiated cathode at the time of battery assembly, eliminating the need to handle metallic lithium. Charging of an anode-free battery results in the deposition of lithium metal between the solid electrolyte and the anode current collector. Unfortunately, there are many challenges to realizing the uniform plating and stripping of lithium metal.[2−6] Surface inhomogeneities and poor wetting thermodynamics can cause ionic and electronic current hotspots that lead to dendrite growth during charging and void formation during stripping.[7−9] This has motivated a search for interphase layers and surface treatments that are able to facilitate reversible and uniform Li deposition and stripping.

Metallic alloying elements, placed between the solid electrolyte and the current collector, have been shown to affect the mechanisms and rates with which Li plates and strips in all-solid-state batteries.[10−21] While the specific role that metal additions play during Li deposition and stripping remains poorly understood, their ability to alloy with Li appears to be crucial. A variety of mechanisms have been proposed in which metallic particles affect Li deposition and stripping. Li reacts with many metals to form intermetallic compounds. These may wet the solid-electrolyte surface and thereby improve the bonding between metallic lithium and the solid electrolyte.[22−25] An intermetallic that wets the solid electrolyte surface must exhibit a high Li mobility to allow for Li passage. Some Li-metal alloys, such as Li−Mg, form solid solutions instead of intermetallic compounds. Yang et al.[14] have suggested that a Li−Mg solid solution enables a dealloying reaction during Li stripping, thereby leaving behind an interconnected metallic sponge that maintains an electronic connection between the solid electrolyte surface and the anode current collector for subsequent Li deposition. Choi et al.[26] also demonstrated that dilute additions of Mg to the anode alters the morphology of Li upon plating, improving the cyclability of all-solid-state batteries. A uniform dispersion of metallic particles may also promote the nucleation of Li-rich phases at potentials above that of Li metal formation, thereby eliminating the need of a nucleation overpotential once the potential at the solid electrolyte interface has reached that of pure metallic Li.[20,27,28]

Received: May 4, 2024
Revised: July 10, 2024
Accepted: July 11, 2024
Published: July 30, 2024

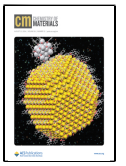

Lithium alloys are unique in many ways, yet their basic thermodynamic, kinetic, and mechanical properties remain to be determined and understood. Here we survey fundamental properties of lithium alloys using first-principles electronic structure calculations. The energy surface of lithium metal along crystallographic deformation paths that connect BCC to close-packed phases such as HCP and FCC is unusually flat and anharmonic. This has fundamental implications about the true nature of the room temperature BCC form of lithium metal and about its deformation mechanisms. The migration barriers for Li hops into neighboring vacancies in BCC, FCC, and HCP are predicted to be unusually low, but the cost to form vacancies is high and comparable to that of other metals. Hence, vacancies are rare, but once present are exceptionally mobile in lithium metal. We next focus on the thermodynamic and kinetic properties of the Li−Mg alloy, which forms a BCC solid solution. Here as well, migration barriers for diffusion are predicted to be exceptionally low, but vacancies are dilute due to their high formation energies. Kinetic Monte Carlo simulations predict that the addition of Mg to BCC Li leads to a reduction of the tracer diffusion coefficients by an order of magnitude. In contrast to the Li−Mg alloy, most Li-M binary phase diagrams contain a wide variety of intermetallic compounds. We show that many Li-M intermetallics are orderings of Li and metal over the sites of a BCC parent crystal structure. Furthermore, important intermetallic crystal structures can be generated algorithmically from the C49 Li_2M structure upon introducing a periodic array of antiphase boundaries. This results in local networks of Li sites that are interconnected by nearest-neighbor hops, with beneficial consequences for Li diffusion mechanisms. Of the intermetallic compound formers, we focus on Ag, Zn, Al, Ga, In, Sn, Sb, and Bi as these have shown promise in fostering lithium plating and stripping in all-solid-state battery configurations. Unusually low migration barriers are predicted in most Li-intermetallic compounds investigated in this work. Vacancies, which are crucial in mediating substitutional diffusion, in contrast, have high formation energies in most Li-intermetallic compounds. However, several intermetallic compounds, including B32 LiAl and LiGa as well as $D0_3$ Li_3Sb and Li_3Bi, are predicted to host structural vacancies at high concentrations. These compounds, therefore, belong to a class of unique intermetallics that are characterized by exceptionally high Li mobilities.

2. METHODS

First-principles density functional theory (DFT) was used to calculate the energies and to analyze the electronic structures of intermetallic compounds in Li-M binary alloys, where M was chosen to be Mg, Ca, Ag, Zn, Al, Ga, In, Sn, Sb, and Bi. All first-principles calculations were performed within the GGA-PBE[29] approximation of DFT using the Vienna Ab initio Simulation Package (VASP).[30−32] The projector augmented wave method[33] pseudopotentials, Li_{sv}, Mg, Ca_{sv}, Ag, Zn, Al, Ga_d, In_d, Sn_d, Sb, and Bi_d were used for the calculations. A plane-wave energy cutoff of 650 eV and an automatic Γ-centered k-point grid with a length parameter R_k of 64 were used for all the calculations to keep the error within 1 meV/atom. Gaussian smearing with a smearing width of 0.02 eV was used while performing geometric relaxations. Subsequently, the tetrahedron method with Blöchl corrections was used in a final static calculation of the total energies. The energies and forces were converged with a cutoff criterion of 10^{-5} eV and 0.02 eV/Å respectively.

Migration barriers for atomic hops were calculated using the nudged elastic band (NEB) method as implemented within the Transition State Tools for VASP (VTST-Tools).[34−36] A climbing image method with a quick-min optimizer was used to accurately determine the energy of the transition state. All the energies were converged within 10^{-5} eV and the forces within 0.03 eV/Å. The NEB calculations were performed using large supercells containing 128 atoms or 108 atoms depending on the ordering of the intermetallic compound. All the symmetrically unique atomic hops in a supercell were enumerated with the CASM software package.[37] Vacancy formation energies were also calculated by placing a vacancy in large supercells containing different arrangements of Li and M atoms. There is no unique definition of a vacancy formation energy in an alloy[38,39] due to the ambiguity as to which chemical species occupied the site of the crystal that is made vacant. A meaningful definition of a vacancy formation energy in a multicomponent crystal should be formulated in the grand canonical ensemble since the composition of the solid changes upon the introduction of a vacancy. Within the grand canonical ensemble of a solid with a fixed number of crystal sites, the chemical potentials are held constant and a vacancy formation energy can be defined according to

$$\Delta\Omega = E(N_{Va} = 1) - E(N_{Va} = 0) - \Delta N_{Li}\mu_{Li} - \Delta N_M\mu_M \quad (1)$$

where $E(N_{Va} = 1)$ is the energy of a large supercell of the compound containing one vacancy, while $E(N_{Va} = 0)$ is the energy of the defect-free compound. The ΔN_{Li} and ΔN_M are either equal to −1 or 0, depending on whether a Li or M is removed from the compound to form the vacancy. The compound is assumed to be in equilibrium with a reservoir of Li and M having chemical potentials μ_{Li} and μ_M, respectively. Due to the Gibbs−Duhem relationship, the chemical potentials of Li and M are not independent, but are instead related according to $\mu_M = (g(x) - x\mu_{Li})/(1 - x)$, where $g(x)$ is the Gibbs free energy per atom of the compound at a composition $x = N_{Li}/(N_{Li} + N_M)$. For intermetallic compounds that exhibit minimal disorder, the free energy $g(x)$ can be approximated by their energy $(e(x)=E(N_{Va} = 0)/(N_{Li}+N_M))$.

The equilibrium thermodynamic voltage (V) is defined according to the Nernst equation as follows,

$$V = -\frac{\mu_{\mathrm{Li}} - \mu^{\circ}_{\mathrm{Li}}}{e} \quad (2)$$

where μ_{Li} is the chemical potential of Li, $\mu^{\circ}_{\mathrm{Li}}$ is the chemical potential of the reference electrode, and e is the charge of an electron.[40] In a binary alloy, the chemical potential of Li can be related to the Gibbs free energy per atom (g) according to

$$\mu_{\mathrm{Li}} = g + \frac{\partial g}{\partial x_{\mathrm{Li}}}(1 - x_{\mathrm{Li}}) \quad (3)$$

Statistical mechanics approaches that rely on cluster expansion surrogate models[41,42] and Monte Carlo (MC) simulations as implemented in the CASM software package[37,43,44] were used to calculate room temperature thermodynamic and kinetic properties of the Li−Mg alloy. A cluster expansion describes the energy of a crystal as a function of the degree of chemical ordering among its constituents and is a powerful surrogate model with which to interpolate DFT formation energies within MC simulations. Translationally invariant cluster expansions were trained to large data sets of DFT formation energies for the BCC and HCP parent crystal structures of the Li−Mg alloy using the techniques described by Ober and Van der Ven.[45] Room temperature thermodynamic properties of the BCC and HCP phases in the Li−Mg system were obtained by performing MC simulations using the trained cluster expansions in the grand canonical ensemble. A supercell size of 10 × 10 × 10 (13 × 13 × 13) of the conventional unit cell of BCC (primitive unit cell of HCP) was used for the MC simulations. The Gibbs energies (g) of the BCC and HCP phases at room temperature were obtained by integrating the results of MC simulations as outlined in Puchala et al.[43] Once the Gibbs energy was obtained, the voltage was determined using eq 3. Vacancies were treated as a ternary species as described by Belak and Van der Ven.[39] Kinetic Monte Carlo simulations (KMC) were performed to calculate tracer diffusion coefficients[46−49] using the CASM software package.[37,43] The equilibrium vacancy concentration at room temperature in the Li−Mg alloy was determined using the

https://doi.org/10.1021/acs.chemmater.4c01279
Chem. Mater. 2024, 36, 7370−7387

method outlined in Belak and Van der Ven.[39] Since the predicted equilibrium vacancy concentration was very low, any interactions between vacancies can be neglected, and the transport coefficients can be scaled linearly with vacancy concentration.[48] The KMC simulations were performed by placing a single vacancy in a 2000 atom supercell of BCC. The obtained kinetic transport coefficients were then scaled to the calculated equilibrium vacancy concentration at room temperature.[48]

3. RESULTS

3.1. Li Metal. Lithium is a highly unusual metal.[50,51] While it adopts the BCC crystal structure at room temperature, it has a very low melting temperature (453 K, or 180 °C) and becomes susceptible to martensitic structural transformations upon cooling below room temperature. The low-temperature phase that BCC lithium transforms to can be one of the many possible close-packed crystal structures, such as FCC, HCP, or 9R, with the adopted stacking sequence depending on the thermal and mechanical history.[50−54] The susceptibility of lithium to transform to a close-packed crystal structure having one of many possible stacking sequences at low temperature is apparent in the zero kelvin energy surface of Li. DFT calculations predict a high degree of degeneracy among a large number of close-packed crystal structures.[50,51] Furthermore, there is a negligible barrier at zero kelvin separating the BCC crystal structure from different close-packed crystal structures.[51]

The unusual nature of the Li metal energy surface is revealed upon inspection of its energy as a function of symmetry-adapted strain order parameters.[51] These are defined in terms of the Cartesian strains, E_{xx}, E_{yy} and E_{zz}, according to[55]

$$e_1 = \frac{1}{\sqrt{3}}(E_{xx} + E_{yy} + E_{zz}) \tag{4}$$

$$e_3 = \frac{1}{\sqrt{6}}(2E_{zz} - E_{xx} - E_{yy}) \tag{5}$$

The strain is measured relative to the BCC crystal structure (i.e., the BCC crystal structure corresponds to zero Cartesian strains). The first strain order parameter, e_1, measures changes in volume, while e_3 measures tetragonal distortions of the BCC crystal along the $\hat{z}$ axis. A positive e_3 transforms the BCC reference crystal to the FCC crystal along the Bain path. A negative e_3 compresses the BCC crystal along the $\hat{z}$ axis and transforms the (110) planes of BCC into triangular layers. Adjacent pairs of the resulting triangular layers can then be shuffled in opposite directions to form the HCP crystal along the Burgers path.[51] Both the Bain and Burgers paths are illustrated in Figure 1.

Figure 2 compares the energy of Al and Mg to that of Li as a function of the two symmetry-adapted strain order parameters, e_1 and e_3. Figure 2a clearly shows a deep well in the energy surface of Al at strains corresponding to the FCC crystal structure, the stable polymorph of Al, while Figure 2b shows a deep well in the energy surface of Mg at strains corresponding to the HCP crystal structure. Neither Al nor Mg are stable in the BCC crystal structure, as manifested by the saddle point in the energy surface at the BCC strain values. The energy surface of Li, shown in Figure 2c, is very distinct from those of Al and Mg, and is remarkably flat as a function of both e_1 and e_3. The energies of BCC, HCP, and FCC Li differ by at most 1 meV per atom, which is within the numerical accuracy of the density functional theory calculations, and there is a negligible barrier

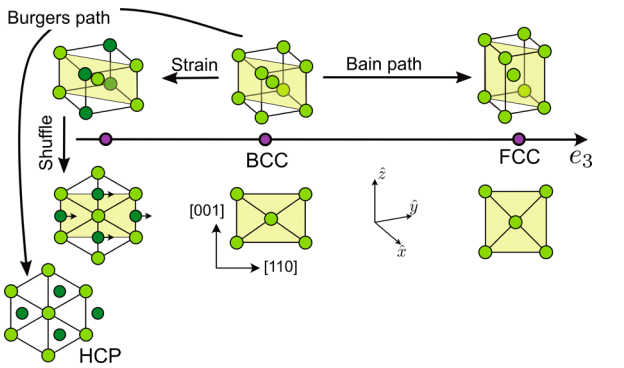

Figure 1. Bain and Burgers paths that connect BCC to FCC and BCC to HCP respectively.

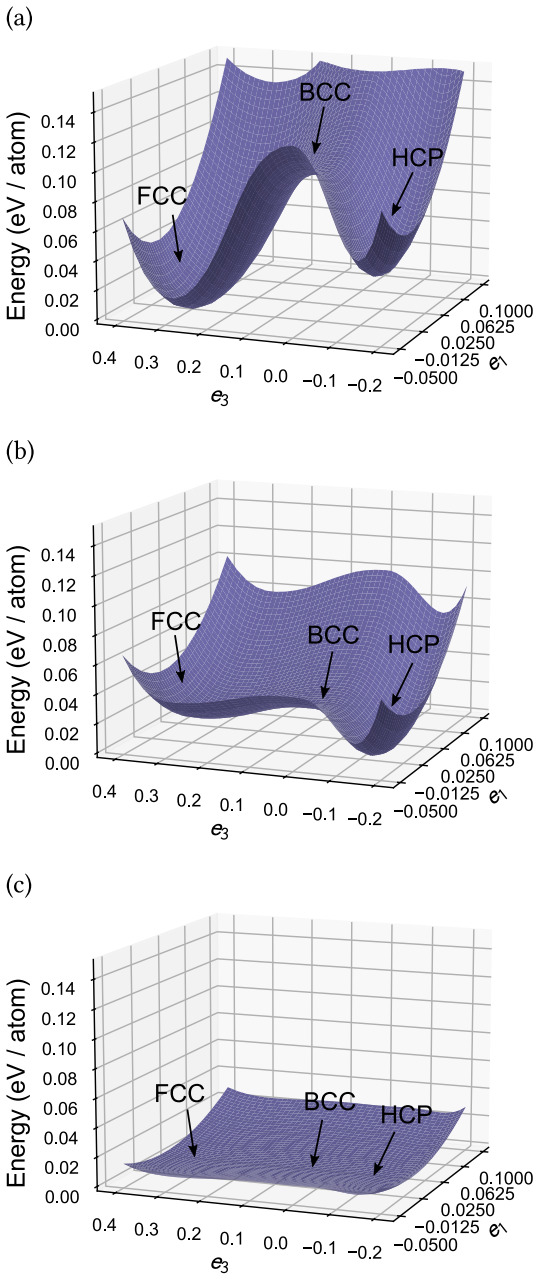

Figure 2. Energy surfaces of (a) Al, (b) Mg and (c) Li as a function of symmetry-adapted strain order parameters e_1 and e_3.

https://doi.org/10.1021/acs.chemmater.4c01279
Chem. Mater. 2024, 36, 7370−7387

separating the different crystal structures. Past DFT calculations have shown that the degeneracy of Li extends beyond BCC, HCP, and FCC and includes most close-packed crystal structures, including DHCP and 9R.[50,51] The unusually flat energy surface of lithium at zero kelvin, of which a small portion is shown in Figure 2c, raises fundamental questions about the true nature of the local structure of the BCC phase of lithium at room temperature. The room temperature BCC phase may be an entropically stabilized crystal, in which anharmonic vibrational excitations stabilize the high symmetry BCC crystal structure,[56,57] in spite of the zero kelvin near-degeneracy in energy with the infinitely large family of close-packed crystal structures. This implies that the elastic properties of the BCC phase should be very sensitive to temperature. An alternative model of the local structure of the room-temperature BCC form of Li could consist of many different orientational and stacking ordered variants of close-packed phases coexisting at the nanoscale that collectively diffract as a high temperature BCC crystal.

The barriers for Li migration within different polymorphs of Li are also unusually low.[58,59] Figure 3a shows the migration barrier for a nearest neighbor Li hop into an adjacent vacancy within the BCC crystal structure. This energy was calculated with the nudged-elastic band method in a 128 atom supercell. The barrier for a nearest neighbor hop is predicted to be only ~35 meV, an exceedingly low value. Figure 3a shows the energy for a second-nearest neighbor hop. The barrier of ~215 meV is slightly higher than that of the nearest neighbor hop, but is nevertheless unusually low compared to the migration barriers of other elemental metals.[46,49,60−62] Figure 3b shows the energies for nearest neighbor hops in the FCC and HCP forms of Li. Here as well, the barriers are very low, having values that range between 120 and 150 meV.

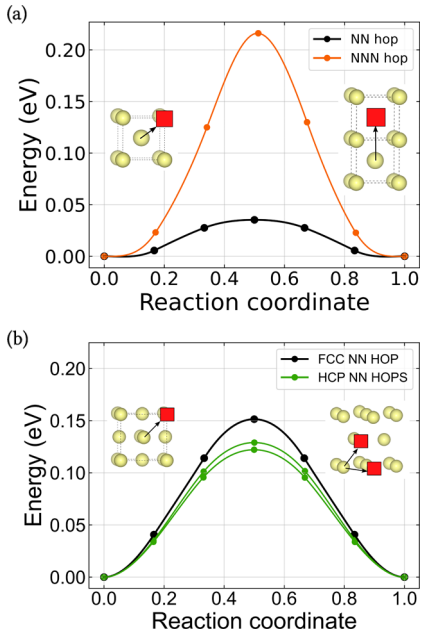

Figure 3. (a) Li - Va nearest neighbor hop and next-nearest neighbor barrier energy in BCC. (b) Li - Va nearest neighbor hop barrier energy in FCC and HCP. The calculations for BCC and HCP are carried out in a 128 atom supercell whereas a 108 atom supercell is used for FCC. NN and NNN represent lithium hopping to a nearest neighbor and a next(second)-nearest neighbor vacant site, respectively.

While the migration barriers for Li hops in BCC, FCC, and HCP are very low, macroscopic diffusion requires the presence of an abundant concentration of vacancies.[48,49,63] The vacancy formation energy, ΔE_V, in BCC Li (as calculated using a 128 atom supercell) is 0.544 eV, which is consistent with previous calculations.[58,59] The calculated vacancy formation energies in the close-packed FCC and HCP crystal structures are somewhat higher, having values of 0.614 and 0.633 eV, respectively. The equilibrium vacancy concentration, x_V, at room temperature can be estimated using $x_V = e^{-\Delta E_V/k_B T}$, where k_B is Boltzmann's constant and T is the temperature. Using the BCC vacancy formation energy, the equilibrium vacancy concentration at room temperature is of the order of 6.63×10^{-10}, a very low concentration. The reported vacancy concentration is purely estimated based on the vacancy formation energy and does not include contributions from vibrational excitations. This may change the equilibrium vacancy concentration but not more than one or two orders of magnitude.[58,59,61,64] This very dilute vacancy concentration results in a low Li tracer diffusion coefficient in spite of the unusually low migration barrier for Li hops. The activation barrier for diffusion, calculated as the sum of the vacancy formation energy and the nearest neighbor hop barrier (0.57 eV), is consistent with that extracted from tracer diffusion coefficient measurements.[65] While high, the zero kelvin calculations of migration barriers indicate that once a vacancy is present in lithium metal, it should be exceptionally mobile.

3.2. Alloys That Form Solid Solutions: The Li−Mg Alloy. Magnesium has been studied as a metal additive to anode-free solid-state battery architectures.[13,14,66] The Li−Mg alloy is experimentally well characterized[67] and is known to form a large solid solution on the BCC parent crystal structure between $x \approx 0.3$ and $x = 1$. Pure Mg and dilute Li_xMg_{1-x} alloys, in contrast, adopt the HCP parent crystal. First-principles DFT calculations predict similar behavior, with different orderings of Li and Mg over the sites of the BCC parent crystal being stable above $x = 1/3$ and pure Mg favoring the HCP crystal structure. Figure S15 of the Supporting Information shows the formation energies of 630 (223) different Li−Mg orderings over the sites of the BCC (HCP) parent crystal structure. Most orderings have negative formation energies with many residing on or very close to the convex hull.

In addition to comparing the formation energies of different Li−Mg arrangements on the BCC and HCP parent crystal structures, it is instructive to analyze the variation of the energy of several configurations on the convex hull along the Bain and Burgers paths. Figure 4a clearly shows that the addition of Mg to BCC Li leads to an increase in the curvature of the energy along the Bain and Burgers paths at $e_3 = 0$, corresponding to the BCC phase. As described above, the energy of pure Li along the Bain and Burgers paths is unusually flat, with BCC, FCC, and HCP being degenerate in energy within the accuracy of the DFT calculations. A dilute addition of Mg leads to a slight change in the energy surface along the Bain and Burgers paths, as is evident for the lowest energy arrangement of Li and Mg at $x = 0.833$. While BCC (at $e_3 = 0$) has become a clear minimum at $x = 0.833$, the energies of the FCC and HCP forms of this ordering are only slightly above that of BCC. At $x = 0.5$, however, the lowest energy arrangement of Li and Mg

https://doi.org/10.1021/acs.chemmater.4c01279
Chem. Mater. 2024, 36, 7370−7387

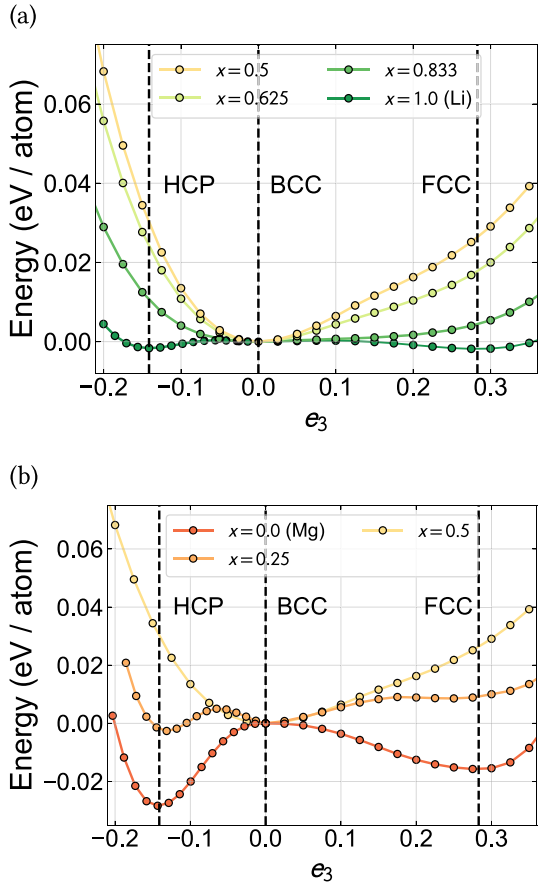

Figure 4. Energy along Bain and Burgers path for various orderings in the Li_xMg_{1-x} binary system for (a) $x \geq 0.5$, (b) $x \leq 0.5$. The Li−Mg orderings are either ground states or structures within 5 meV/atom from the global convex hull as calculated with DFT.

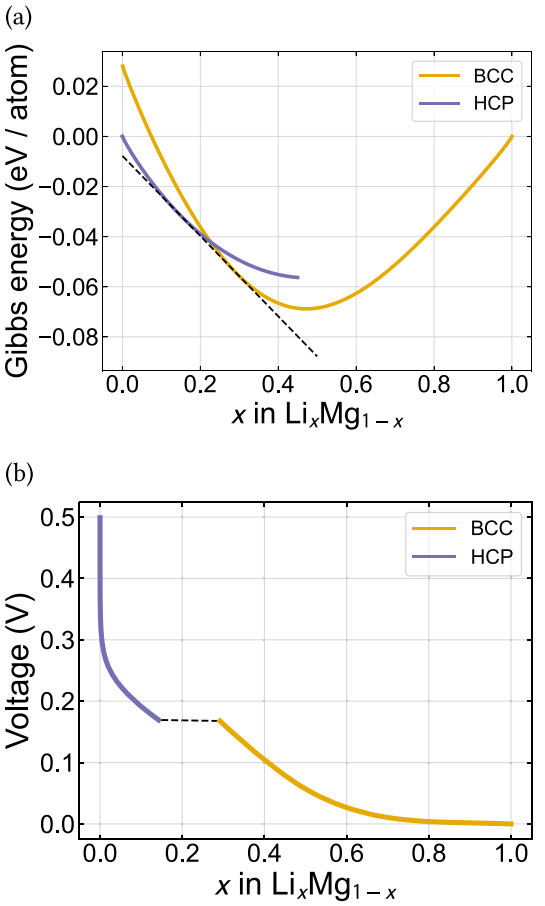

Figure 5. Room temperature (a) Gibbs free energy and (b) voltage in Li−Mg binary system.

on the BCC parent crystal structure, which corresponds to the CsCl B2 ordering, exhibits a clear minimum in the BCC phase. Figure 4b shows that as the Mg concentration increases, the BCC phase progressively becomes less stable and even unstable, while the local minimum corresponding to HCP decreases to become the globally stable state in pure Mg at $x = 0$.

While the BCC form of Li−Mg is unusually anharmonic and only marginally stable with respect to the Bain and Burgers transformations to FCC and HCP, respectively, at high Li concentrations, we nevertheless explored the configurational thermodynamics of the BCC alloy at finite temperature, neglecting the effects of anharmonic vibrational excitations.[56,57] The fully relaxed formation energies were used to train cluster expansions of the configurational energies of the BCC and HCP parent crystal structures of Li_xMg_{1-x}. The cluster expansions were implemented in Monte Carlo simulations to calculate free energies and voltage curves at and around room temperature. Figure 5 shows the free energy of the Li_xMg_{1-x} alloy and voltage curve with respect to a lithium metal reference electrode at room temperature.[40,44] At room temperature, the Li−Mg alloy forms a uniform solid solution in the BCC phase between $x = 0.292$ and 1. At dilute Li concentrations, the alloy is stable in the HCP phase. The voltage is very low at Li-rich concentrations and rises rapidly below $x = 0.5$. The transition from the BCC solid solution to the Mg-rich HCP solid solution is manifested by the plateau in the voltage curve predicted to occur at 0.169 V.

The addition of alloying elements to a metal will not only modify the thermodynamic properties of the pure metal but also its kinetic properties. For example, alloying elements can modify the equilibrium vacancy concentration and affect migration barriers for diffusion.[39,68] Furthermore, alloying elements may either attract or repel vacancies, which can lead to highly correlated diffusion that generally results in a reduction of the diffusion coefficient.[46,48,49] A first estimate of the effect of an alloying element on diffusion kinetics becomes evident upon inspection of migration barriers in representative environments as a function of alloy concentration. In an alloy such as BCC Li−Mg, the end states of an atomic hop are generally not equivalent, as the hop leads to a rearrangement of the Li−Mg decoration on the BCC lattice. As a result, the energies of the end states are usually not the same and the migration barrier for the hop becomes a function of the direction of the hop as schematically illustrated in Figure 6. To separate out the thermodynamic contributions to the migration barrier, it is convenient to inspect the kinetically resolved activation (KRA) barrier[40,44,69] defined as the average between the forward and reverse hops. Figure 7a collects KRA barriers for the first and second nearest neighbor hops at multiple concentrations in a BCC Li−Mg alloy. The barriers of a total of 16 (17) Li (Mg) hops were calculated in supercells containing 128 atoms using the nudged elastic band method. Figure 7a clearly shows that the nearest neighbor hops of both

https://doi.org/10.1021/acs.chemmater.4c01279
Chem. Mater. 2024, 36, 7370−7387

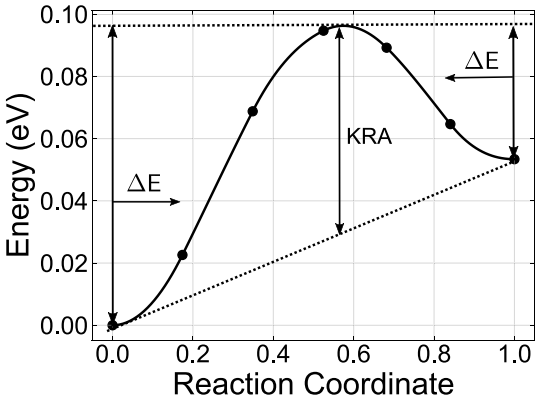

Figure 6. A schematic of a kinetically resolved activation barrier.

Li and Mg in the BCC Li−Mg alloy remain unusually low, having values that fluctuate around 75 meV as indicated by the dashed line in Figure 7a. While the KRA barriers for Li are overall slightly smaller than those of Mg, the difference is negligible compared to k_BT at room temperature. The addition of Mg, therefore, appears to have a negligible effect on the nearest neighbor hop barriers of vacancies. The KRA barriers for the second nearest neighbor hops (as indicated by NNN Figure 7a) in BCC Li−Mg, in contrast, are very sensitive to the alloy concentration, steadily increasing as the alloy becomes richer in Mg.

The addition of Mg to BCC Li will also affect the equilibrium vacancy concentration. Figure 7b shows vacancy formation energies as a function of the alloy composition upon the removal of either a Li or a Mg atom at constant chemical potentials μ_{Li} and μ_{Mg}. The vacancy formation energies are defined according to eq 1 and the Li and Mg chemical potentials appearing in eq 1 are taken to be their values in the solid solution at each alloy composition as determined by the BCC free energy of Figure 5a. The addition of Mg does not result in a general reduction of the relatively high vacancy formation energy of pure Li.

Room temperature diffusion coefficients can be calculated with kinetic Monte Carlo simulations using cluster expansion techniques to describe the energies of the end states and activated states in a disordered alloy.[38,39,46,48,49,70,71] The approach relies on a cluster expansion for the end states of each hop that is combined with a local cluster expansion of the KRA barriers.[40,44] A constant KRA of 75 meV, along with a vibrational prefactor of 10^{13} Hertz, was used for nearest neighbor hops of lithium and magnesium within the KMC simulations. Figure 7c shows the calculated tracer diffusion coefficients of Li and Mg as a function of alloy composition normalized by the Li tracer diffusion coefficient at $x = 1$. Since the energy landscape of Li is highly anharmonic, methods beyond the standard transition state theory are required to compute the vibrational prefactor accurately.[72] Nevertheless, we can accurately estimate the relative changes in tracer diffusion coefficients using an approximate vibrational prefactor, as any errors arising from the vibrational prefactor will be systematic. Using the aforementioned vibrational prefactor in KMC simulations, the tracer diffusion of coefficient of lithium at $x = 1$ is predicted to be 5.455×10^{-13} cm^2/s with an approximate equilibrium vacancy concentration of 1.16×10^{-9}. The tracer diffusion coefficients of Li and Mg are very similar, in large part due to the fact that their KRA barriers are very similar. A reduction by 1 order of magnitude in both tracer diffusion coefficients with increasing Mg composition is predicted. This is in agreement with experimental measurements,[66] which also report a decrease in

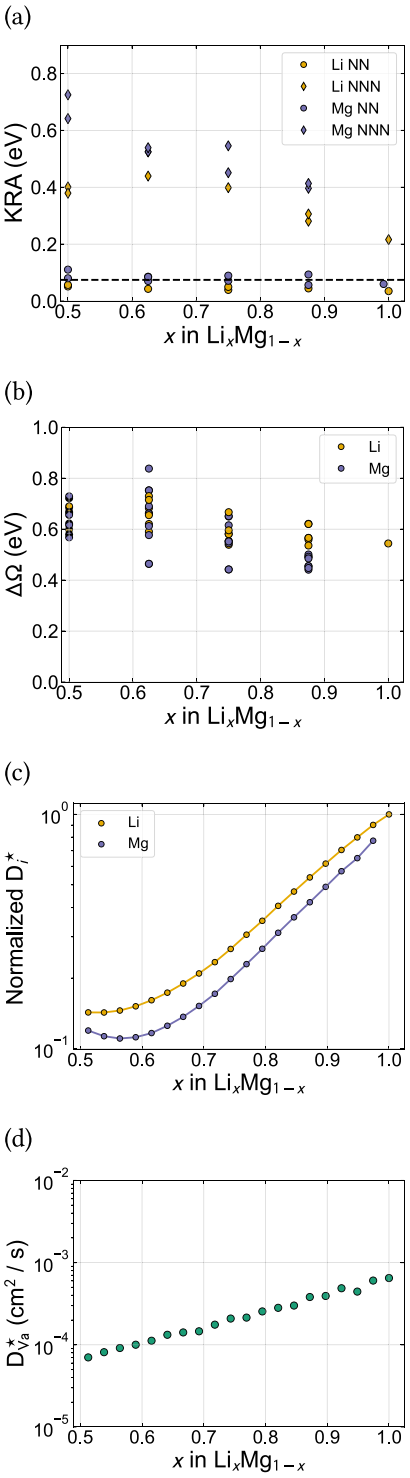

Figure 7. (a) Kinetically resolved activation (KRA) barriers as a function of lithium composition. NN and NNN denote Li/Mg hopping to a vacant nearest neighbor and next(second)-nearest neighbor site, respectively. (b) Grand canonical vacancy formation energies as a function of composition. (c) Tracer diffusion coefficients of Li, Mg normalized with obtained tracer diffusion coefficient of Li as a function of composition. (d) Vacancy tracer diffusion coefficient as a function of composition.

https://doi.org/10.1021/acs.chemmater.4c01279
Chem. Mater. 2024, 36, 7370−7387

diffusion coefficients with increasing Mg content. Figure 7d shows the vacancy tracer diffusion coefficient as a function of alloy composition. The vacancy tracer diffusion coefficient is 9 orders of magnitude larger than the tracer diffusion coefficients of Li and Mg, which suggests that vacancies are very mobile once they are present in the crystal. Similar to the tracer diffusion coefficients of Li and Mg, the vacancy tracer diffusion coefficient is also predicted to decrease by an order of magnitude with the addition of Mg to the alloy. While the addition of Mg to BCC Li does not have a significant effect on migration barriers or vacancy formation energies, it does result in short-range order between Li, Mg, and vacancies. An in-depth analysis of the effects of short-range order on the calculated tracer diffusion coefficients, to be published elsewhere,[73] shows that it leads to correlations between successive vacancy and atom hops that restricts their trajectories compared to that of a purely random walker. The increase in short-range order with an increasing Mg concentration, therefore, leads to a reduction in the tracer diffusion coefficients. The strong effect of short-range order on substitutional diffusion is common in many alloys.[46,49]

3.3. Intermetallic Crystal Structures in Li−M Binaries.

Lithium forms a wide variety of intermetallic compounds with different metallic elements, M. Their structures can be very diverse, but a large number of Li-rich intermetallic phases can be viewed as a particular ordering of Li and M over the sites of a BCC parent crystal structure. Even among the BCC-based intermetallic compounds there is a tremendous diversity of long-range order. Nevertheless, an underlying pattern can be discerned that enables a hierarchical organization among most of the BCC-based Li-M intermetallic compounds.

There are two especially important and common Li-M intermetallics with compositions that straddle the composition interval in which most other Li-M intermetallics form. The first has an equiatomic composition of Li and metal and has the B32 crystal structure. It is formed by LiAl, LiGa, and LiZn. The B32 structure differs from the B2 structure, the most common equiatomic ordered compound on the BCC lattice,[74] in that the Li and metal sublattices of B32 form a nearest-neighbor interconnected network. The other common Li-M intermetallic has the Li_3M stoichiometry and adopts the $D0_3$ crystal structure. This structure can also be viewed as an ordering of Li and M over the sites of the BCC lattice, but the sublattice of M atoms forms an FCC lattice. $D0_3$ is the stable intermetallic structure of Li_3Sb, Li_3Bi, and Li_3In as predicted by zero kelvin DFT calculations (Figure S1 of the Supporting Information).

While less common, the Li_2M C49 intermetallic, formed by Li_2Al, has a structure from which many of the other Li-M intermetallic compounds can be generated through the introduction of antiphase boundaries. The structure of the BCC based Li_2Al ordering can be described as a stacking of a honeycomb-like ordering on the (110) planes of the BCC parent lattice, shown in Figure 8a. The Li-M ordering within the (110) planes is illustrated in Figure 8b. The Li atoms occupy sites in the BCC (110) planes that form a distorted honeycomb network, while the Al atoms occupy the centers of the Li hexagons. The ratio of Li to metal can be varied within this two-dimensional pattern upon the introduction of metal-rich antiphase boundaries or Li-rich antiphase boundaries as illustrated in Figure 8c. By periodically introducing Li-rich and/or metal-rich antiphase boundaries into the C49 structure, it is possible to generate many of the other Li-M intermetallic compound crystal structures. Figure 9, for example, shows that

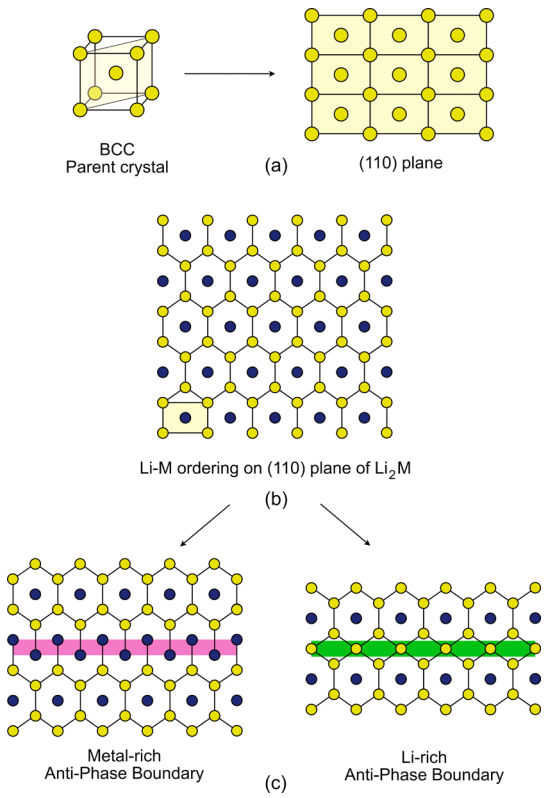

Figure 8. (a) (110) plane in BCC crystal structure. (b) (110) plane of Li_2M ordering. (c) (110) planes of crystal structures containing metal-rich and lithium-rich antiphase boundaries. Li_2M ordering on the (110) plane of BCC can accommodate metal-rich and Li-rich antiphase boundaries to generate a family of intermetallic compounds.

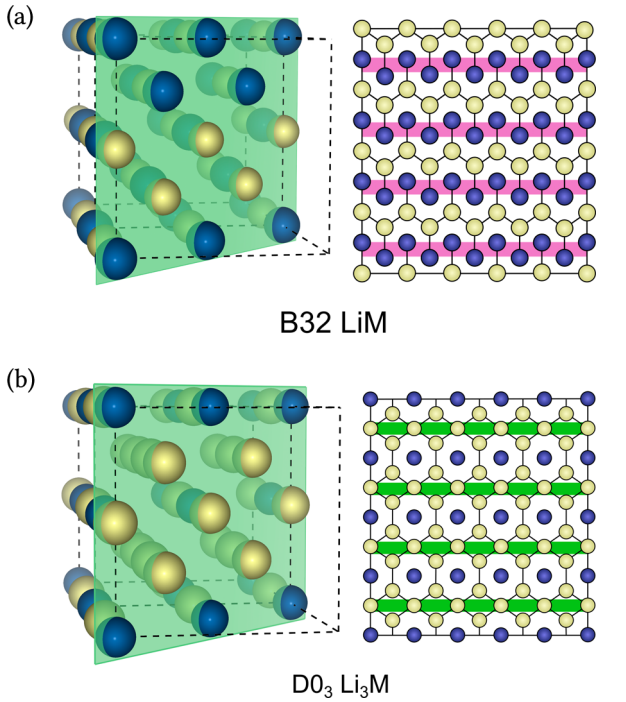

Figure 9. (a) B32 crystal structure with *metal-rich* APBs (b) $D0_3$ crystal structure with *lithium-rich* APBs. The (110) plane in the crystal structure is highlighted in green, and the corresponding ordering on the plane is shown beside it. Lithium atoms are indicated in yellow and metal atoms in blue.

https://doi.org/10.1021/acs.chemmater.4c01279
Chem. Mater. 2024, 36, 7370−7387

the B32 structure having a LiM stoichiometry can be generated from the C49 Li_2M crystal structure upon the periodic introduction of metal-rich antiphase boundaries, while the $D0_3$ structure with a Li_3M stoichiometry can be generated by periodically introducing Li-rich antiphase boundaries. Figure S17 of the Supporting Information shows the (110) planes of the BCC parent structure of many other Li-metal intermetallic compounds that can be generated by introducing antiphase boundaries into C49 Li_2M. The algorithmic generation of ordered phases through the insertion of antiphase boundaries in a parent ordering occurs commonly in many materials classes.[75−80]

All the intermetallic crystal structures derived from C49 through the periodic insertion of antiphase boundaries have interconnected Li sublattices, which is important to facilitate Li diffusion through the compound, as vacancy migration can occur exclusively within the Li sublattice without the need of creating antisite defects. Furthermore, the intermetallics derived from C49 all share common local environments, making it possible to determine the dependence of vacancy formation energies and migration barriers on local structure by considering only a subset of the intermetallic phases.

3.4. Thermodynamics: Stability of Key Structures in Each Li−M Binary. While different Li-metal alloys host a wide variety of intermetallic phases, the antiphase boundary motifs that are common to a large fraction of the intermetallic crystal structures make it possible to distill generalized trends by studying the properties of only a small subset of representative crystal structures. The first is the Li_2Al crystal structure, which consists of distorted honeycomb Li sublattices on the (110) planes of a BCC crystal structure (Figure 8). Two representative structures containing metal-rich and Li-rich antiphase boundaries are the B32 phase, also known as the zintl phase adopted by LiAl, and the $D0_3$ phase, adopted by Li_3Sb, respectively. We also consider the B2 LiM compound, since it is the most common intermetallic ordering on the BCC lattice and has crystallographic features that distinguish it from the B32 phase.[74] As metallic alloying elements, M, we focus on Ag, Zn, Al, Ga, In, Sn, Sb, and Bi.

Figure 10 summarizes the degree with which the B32, B2, C49, and $D0_3$ intermetallic crystal structures are stable for each alloy. The color denotes the extent to which each intermetallic is stable relative to the convex hull of stable intermetallics of the alloy. Green indicates that the compound is stable or marginally metastable and red signifies that the compound has a formation energy well above the global convex hull. Also shown for each alloying element is the energy difference between the formation energy of the compound and the convex hull, expressed in eV/atom. The global convex hull for each alloy was determined by enumerating approximately 632 orderings on the BCC lattice using the CASM software package[37] and performing DFT calculations to obtain their formation energies at zero kelvin. For each Li-M binary considered in this work, we also calculated the energies of other stable or metastable intermetallic compounds that are chemical orderings on parent crystal structures that differ from BCC.[74] These structures were taken from the Materials Project database.[81] Figures S1 and S2 of the Supporting Information collect zero kelvin convex hulls and voltages for all the binary systems considered in this work.

Figure 10a shows that the B32 LiM crystal structure is favored by Zn, Al, and Ga. The B32 LiAl and LiGa compounds have the peculiar property that their energy is lowered upon

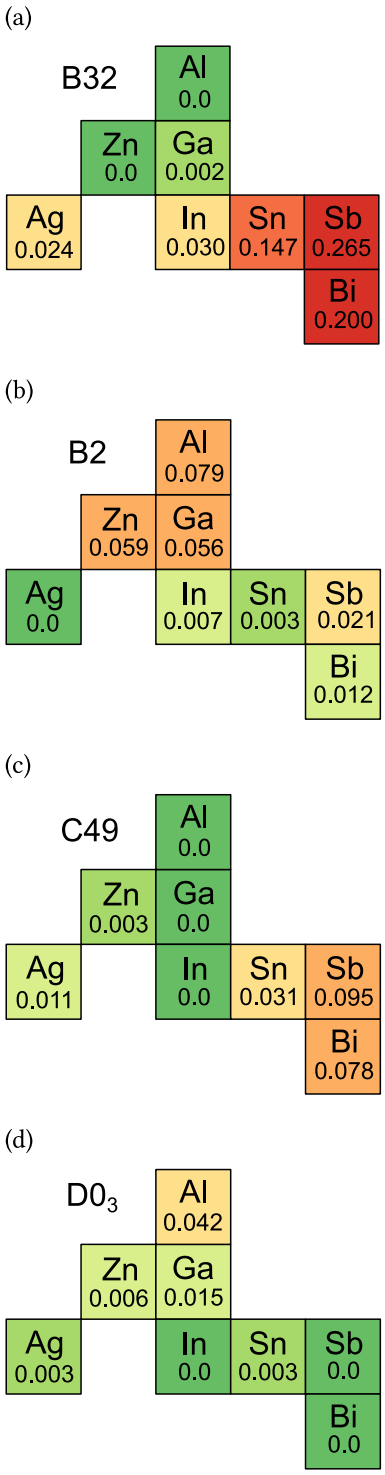

Figure 10. Distances (eV/atom) from the global convex hull in respective Li-M binaries for (a) B32, (b) B2, (c) C49, and (d) $D0_3$ crystal structures. Of these structures, only those within 10 meV/atom from the global convex hull are picked to study diffusion. In calculating the global convex hull, only the perfect stoichiometric B32 and $D0_3$ crystal structures were included and B32 or $D0_3$ crystal structures containing defects were excluded.

the introduction of vacancies on the Li sublattice or Li antisites on the Al/Ga sublattice. Figures S18 and S19 of the Supporting Information show that the formation energies of structures containing a dilute concentration of Li vacancies on the Li sublattice (approximately 2.5% in total or 5% on the

https://doi.org/10.1021/acs.chemmater.4c01279
Chem. Mater. 2024, 36, 7370−7387

lithium sublattice) or Li antisite atoms on the Al/Ga sublattice of the B32 LiAl and LiGa compounds reside on the convex hull and that the perfectly ordered compounds are slightly above the convex hull. In the next section, we show that this behavior has a clear origin in the electronic structure of the B32 LiAl and LiGa compounds. Alloying elements such as Sn, Sb, and Bi are highly unstable in the B32 crystal structure. An opposite trend across the limited periodic table of Figure 10 is evident for the B2 crystal structure (Figure 10b). While only LiAg in the B2 structure is on the global convex hull, the B2 forms of LiIn, LiSn, LiSb, and LiBi are much closer to the global convex hull of each alloy than the B32 structure. As shown in Figure 10c, the C49 Li_2M intermetallic crystal structure is on the convex hull for the Li−Al, Li−Ga, and Li−In alloys and is almost stable for the Li−Zn alloy. The C49 structure is unstable in the Sn, Sb, and Bi alloys. Finally, the $D0_3$ Li_3M compound is favored by most alloys considered here, being on the convex hulls in the In, Sb, and Bi alloys and within 3 meV/atom of the convex hull for Ag and Sn. Only in the Li−Al alloy is $D0_3$ distant from the convex hull.

An important property in solid-state batteries is the extent to which the volume increases as Li reacts with different metal additives. Figure 11 shows the change in volume of the stable

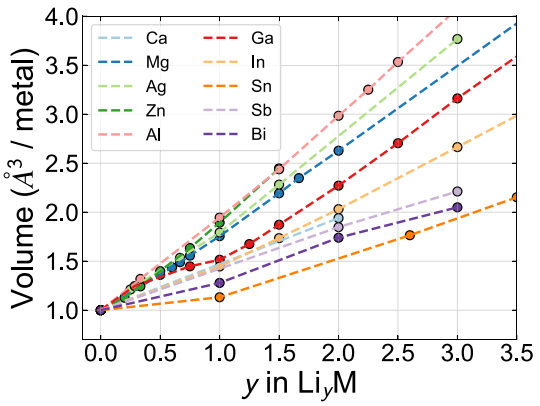

Figure 11. Normalized volume per metal atom of various lithium intermetallic compounds.

Li_yM intermetallic compounds as a function of the Li to M ratio, y, relative to the original volume of the pure metal M. Ag, Zn, Mg, and Al approximately double their volume upon forming their stable LiM compounds with $y = 1$. The compounds that form when Li alloys with Sn exhibit the smallest relative volume change. This is because pure Sn adopts the open, low density diamond crystal structure, while the Li−Sn intermetallic phases are different orderings of Li and Sn over either close-packed structures or the BCC parent crystal structure. The relative volume changes when Li reacts with Bi are also small compared to the other metals. Figure S16 in the Supporting Information shows the change in absolute volume of all the intermetallic compounds as a function of Li to M ratio, y. As depicted in the figure, the absolute volumes of Sn and Bi are higher than most of the other metals under consideration.

3.5. Electronic Structure of the Zintl B32 Intermetallics. While there are often many factors that contribute to the stability of a particular intermetallic compound, the stability of the zintl B32 LiM compound for the metals considered in this work is strongly rooted in the electronic structure of the compound. Figure 12a shows the electronic density of states

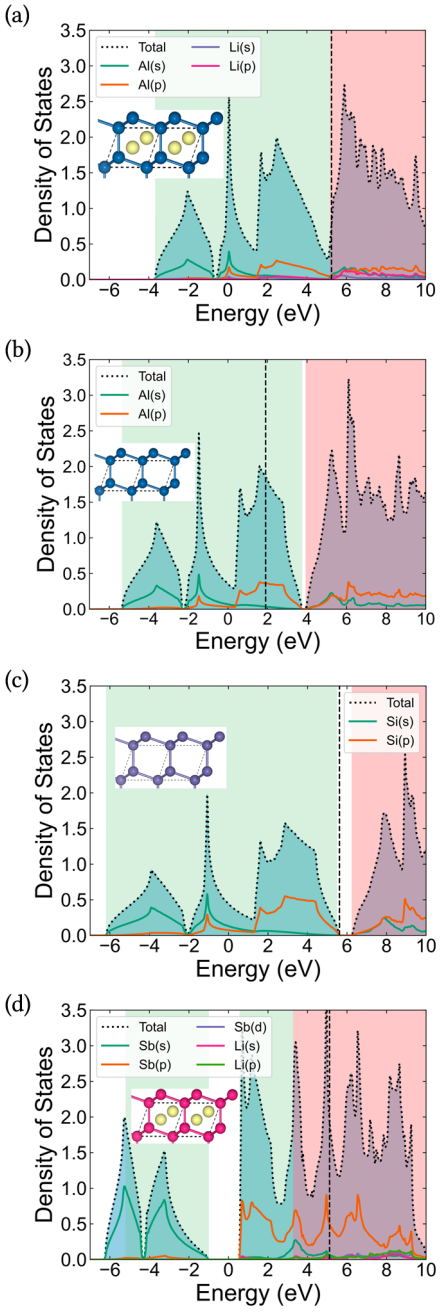

Figure 12. Density of states of (a) B32 LiAl, (b) B32 LiAl with lithium taken out from the crystal structure, (c) diamond cubic Si, and (d) B32 LiSb. Bonding and antibonding regions of the Metal − Metal bonds are shaded with green and red, respectively. Figure S14 in the Supporting Information illustrates the COHP analysis used to determine the bonding and antibonding regions.

(DOS) for B32 LiAl. The compound is predicted to be a semimetal, with a small overlap between the bonding valence bands and antibonding conduction bands.[82] The partial density of states projected on the Al and Li s and p orbitals indicates that the bands derived from Li orbitals reside above the Fermi level (vertical dashed line), while the overwhelming majority of states below the Fermi level derive from the hybridization among Al valence orbitals. The Al in B32 LiM adopts a diamond sublattice. The B32 LiM structure can therefore be viewed as a metal diamond host containing Li interstitials. In this context, it is revealing to compare the DOS

https://doi.org/10.1021/acs.chemmater.4c01279
Chem. Mater. 2024, 36, 7370−7387

of B32 LiAl to that of a hypothetical diamond Al crystal (without Li) having the same lattice parameter as the LiAl compound, shown in Figure 12b. The DOS of the two structures are qualitatively very similar, differing only by the position of the Fermi level and the existence of a small band gap. A comparison of the hypothetical diamond Al DOS to that of diamond Si (Figure 12c), an element to the right of Al in the periodic table, shows a striking similarity as well, differing mostly by the position of the Fermi level. Si adopts the diamond crystal structure as it has exactly four valence electrons to fill all the bonding states derived from the hybridization between its valence s and p orbitals, while keeping the antibonding states that constitute the conduction band of Si empty. Al, with similar s and p valence orbitals, has only three valence electrons and therefore an insufficient number to fully fill its bonding states in the diamond structure. The Li atoms of the B32 LiAl compound do not qualitatively alter the bonding states that hold the diamond structure of the Al sublattice together, and only donate their valence electron to the Al host, thereby raising the Fermi level to the top of the bonding states.

Elements such as Sn, Bi, and Sb also have valence s and p orbitals that can hybridize to form similar bonding and antibonding states as those of Si in the diamond crystal structure. Since these elements reside below or to the right of Si in the periodic table, the incorporation of Li in interstitial sites of their diamond structure to form B32 LiSn, LiBi, and LiSb, leads to an increase in the number of electrons, and a concomitant filling of antibonding states. As is evident in Figure 12d, the density of states for B32 LiSb is similar to that of LiAl B32, except that the Fermi level is well within the antibonding states. Hence, metal elements that are in the same column or to the right of Si will be highly unstable in the B32 LiM compound, as is clearly manifested in Figure 10a.

As described in Section 3.4 and shown in Figure S16 of the Supporting Information, stoichiometric B32 LiAl is not a ground state. Instead, variants of B32 LiAl containing a dilute concentration of structural vacancies on the Li sublattice or Li-antisite atoms on the Al sublattice are preferred. This peculiar type of phase stability, which is also predicted for the B32 LiGa compound, can be traced to the underlying electronic structure of the B32 LiAl and LiGa compounds. A close inspection of the electronic DOS of B32 LiAl shows that the Fermi level of the perfect, stoichiometric compound resides within the antibonding states. This occurs because the insertion of Li into the interstitial sites of the Al diamond crystal structure produces a semimetal,[82] with a partial overlap between the bonding valence bands and the antibonding conduction bands of pure Al in the diamond crystal structure. The Fermi level can be lowered to reduce the occupancy of antibonding states by either introducing vacancies on the Li sublattice, or Li antisite atoms on the Al sublattice. Previous studies by Asada et al.[83] and Kishio et al.[84] also predict similar defect structures and attribute their origins to the electronic structure of B32 LiAl.

3.6. Energy Surfaces of Li−M Intermetallics: The Example of Li−Ag. The addition of alloying elements to BCC Li to form ordered intermetallic compounds has a strong effect on the energy of the crystal along the Bain and Burgers paths. As an example, Figure 13 shows the energy of various Li_xAg_{1-x} orderings on BCC as a function of e_3. The addition of Ag to BCC Li leads to a gradual stiffening of the BCC phase, as manifested by an increase in the curvature of the energy

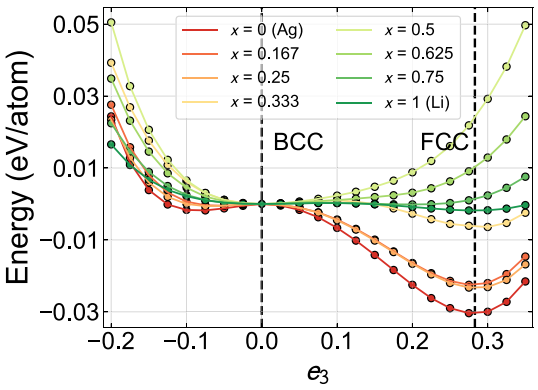

Figure 13. Energy along the Bain path for various Li - Ag orderings.

surface at $e_3 = 0$. The maximum curvature at $e_3 = 0$ occurs at $x = 0.5$ when Li and Ag adopt the B2 ordering on BCC. This compound is also a ground state in the Li_xAg_{1-x} binary. Upon increasing the Ag concentration, the BCC phase becomes unstable (i.e., a negative curvature with respect to e_3) while the FCC phase becomes progressively more stable with respect to the BCC saddle point energy. As with the Li_xMg_{1-x} alloy, the BCC form of Li_xAg_{1-x} at high Li concentrations ($x > 0.5$) is elastically very soft and deformations along the Bain path remain very facile. This property undoubtedly will have important implications for the mechanical properties of Li rich Li_xAg_{1-x} alloys.

3.7. Migration Barriers in Representative Li−M Intermetallic Phases. Diffusion through the crystal structure of an intermetallic compound can be significantly more complex than in dilute alloys or concentrated disordered solid solutions.[46−49,60] The mobility of Li within an intermetallic compound is sensitive to several crystallographic and thermodynamic factors. It depends on the concentration of thermal and/or structural vacancies and the sublattice(s) that vacancies prefer to occupy.[39,60,68] The Li mobility is also very sensitive to the degree with which the Li sublattice sites are interconnected. In the B2 crystal structure, adopted by LiAg, for example, each Li site is coordinated by Ag in its nearest neighbor shell. Hence, any nearest neighbor hop of a Li atom must be to a site on the Ag sublattice, resulting in thermodynamically unfavorable antisite disorder. In contrast to B2, the Li sublattice of the B32 zintl phase forms an interconnected network of sites that can be traversed by nearest neighbor hops. Lithium can therefore migrate through the crystal without increasing the degree of disorder. All intermetallic crystal structures that are derived from the C49 Li_2M structure through the introduction of antiphase boundaries have interconnected Li sublattices and therefore possess the crystallographic prerequisites for favorable Li diffusion characteristics. The metal M of the intermetallic can also diffuse through the crystal and its mobility may be important to preserve the intermetallic crystal structure if high Li fluxes are imposed on the compound.

To determine the degree with which crystal structure and metal chemistry affects Li mobility through intermetallic compounds, we calculated the Li and M migration barriers in the B32, B2, C49 and $D0_3$ crystal structures. Migration barriers were only calculated in intermetallics that are ground states or within 10 meV/atom from the convex hull for a particular Li-M alloy.

https://doi.org/10.1021/acs.chemmater.4c01279
Chem. Mater. 2024, 36, 7370−7387

Figure 14a, shows the migration barriers for Li and Al diffusion within B32 LiAl. The migration barriers are for hops

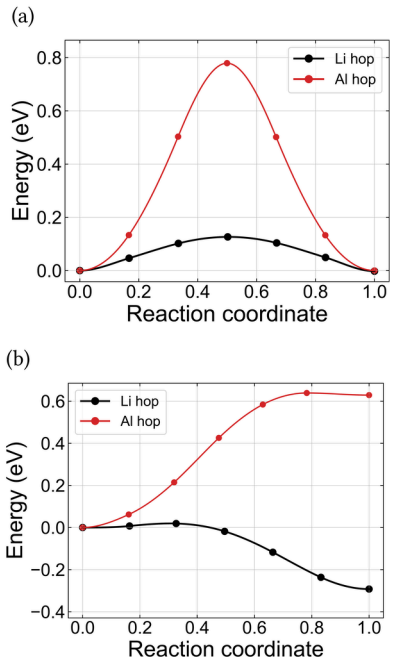

Figure 14. (a) Migration barriers for lithium (black line) and aluminum (red line) hopping to a nearest neighbor vacant site on their own sublattice. (b) Migration barriers for the same lithium (aluminum) hopping to a vacant site on the aluminum (lithium) sublattice.

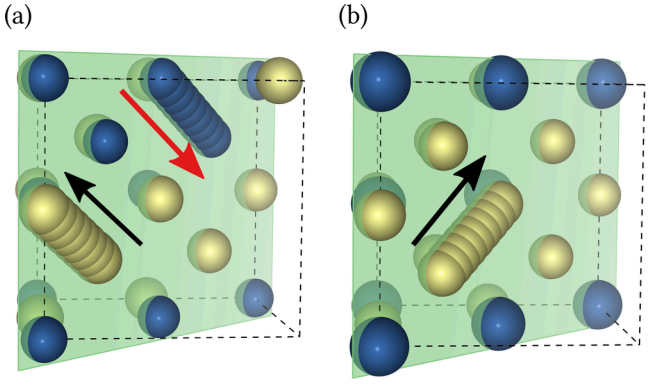

Figure 15. All the symmetrically unique nearest neighbor hops in (a) B32 and (b) $D0_3$ crystal structures. Black arrow represents lithium - vacancy hop, whereas the red arrow represents metal - vacancy hop.

that keep Li and Al on their respective sublattices (Figure 15a). Remarkably, the migration barrier for Li diffusion is very small, being less than 0.15 eV. This barrier is lower than those of the best solid state Li superion conductors.[85−92] The Al migration barrier, in contrast is significantly larger, having a value close to 0.8 eV. These migration barriers indicate that Li diffusion will be exceptionally fast provided that there is a sufficient number of vacancies on the Li sublattice. The Al, which forms the backbone of the compound, in contrast, is not very mobile.

Figure 14b shows migration barriers for antisite hops. The black curve corresponds to a Li hop from the Li sublattice to a vacancy on the Al sublattice. The initial state of this hop consists of one point defect, having a vacancy on the Al sublattice, while the end state consists of two point defects, having a vacancy on the Li sublattice and a Li on the Al sublattice, also referred to as a Li antisite defect. While the hop leads to an increase in the number of point defects, it has a negligible barrier and results in a lowering of the energy of the crystal. This lowering in energy indicates that vacancies are not favored on the Al sublattice and prefer to reside on the Li sublattice, even if it is at the cost of creating a Li antisite. The red curve in Figure 14b shows that an Al hop into a vacancy on the Li sublattice leads to a sizable increase in the energy of the crystal and is highly unstable. These results suggest that Al in B32 LiAl forms a rigid backbone through which Li can diffuse rapidly provided vacancies are available on the Li sublattice. The Supporting Information shows similar plots for B32 LiZn and LiGa. The hop barriers in B32 LiGa are almost identical to those of B32 LiAl, but the antisite hops in B32 LiZn are uphill for both Li and Zn.

While Li migration barriers in stable B32 compounds such as LiAl, LiZn, and LiGa are remarkably low, Li and metal hop mechanisms and barriers are very different in the B2 LiAg compound. In this compound, a nearest neighbor hop of a Li atom to a Ag vacancy is not viable, with the end state of this hop being dynamically unstable as predicted with DFT. A Li attempting to hop to a Ag vacancy will simply roll back to its initial state. In order for a Li ion to hop to a vacant site on the Ag sublattice, it must proceed by a two-atom hop mechanism as illustrated as an inset in Figure 16. A similar mechanism was

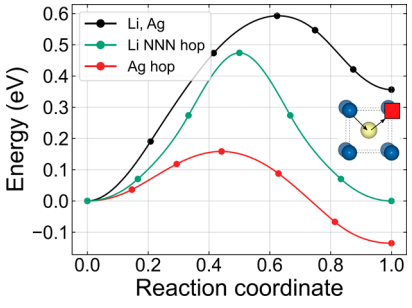

Figure 16. Migration barriers for nearest (NN) and next-nearest neighbor (NNN) hops in B2 LiAg. The Ag atoms are able to perform facile nearest neighbor hops to a vacancy on the Li sublattice. Li nearest neighbor hops, in contrast, are unstable. Li can only migrate to a vacancy on the Ag sublattice by performing a two-atom hop wherein an additional Ag atom moves to avoid creating a vacancy on the Li sublattice. The hop mechanism is shown as an inset, and the corresponding barrier for the hop is shown by the black line labeled (Li, Ag). Li second-nearest neighbor hops have a lower barrier than the two-atom hop.

found necessary to enable nearest neighbor hops in B2 NiAl compounds.[47,60,93] The barrier for this two-atom hop is high, being of the order of 0.415 eV. A Ag atom hopping to a Li vacancy, in contrast, only needs to overcome a kinetically resolved activation barrier of 0.23 eV, as is evident in Figure 16. A Ag atom hopping to a Li vacancy also lowers the total energy of the crystal, suggesting that the vacancy prefers to be on the Ag sublattice. A Li atom in B2 LiAg can also perform second nearest neighbor hops, thereby remaining on the Li sublattice and bypassing the need to create antisite disorder. The barrier for a second nearest neighbor hop, however, is

https://doi.org/10.1021/acs.chemmater.4c01279
Chem. Mater. 2024, 36, 7370−7387

0.475 eV, which is again substantially higher than the Li migration barrier in the B32 LiAl, LiZn, and LiGa compounds. Figure 17 shows migration barriers in C49 Li_2Al. Similar to B32 LiAl, Li hops that stay within the Li sublattice of C49

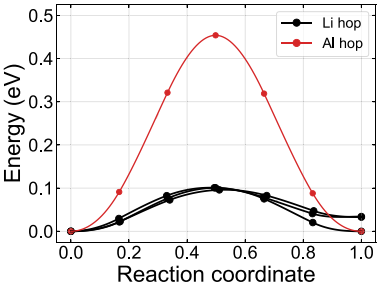

Figure 17. Migration barriers for nearest neighbor hops in C49 Li_2Al.

Li_2Al (black curves) have exceptionally low migration barriers, being of the order of 0.1 eV. In the C49 structure, there are three symmetrically nonequivalent Li nearest neighbor hops. The Al hops within the Al sublattice have a significantly larger migration barrier than those of Li hops, although the barrier of 0.45 eV is almost half of the Al migration barrier within B32 LiAl. As shown in Figure S11 of the Supporting Information, the migration barriers for Li hops in C49 Li_2Al, Li_2Ga, and Li_2In are very similar to each other. Furthermore, the migration barriers of the Al and Ga nearest neighbor hops within their own sublattices are also very similar. The migration barrier of In within C49 Li_2In, in contrast, is significantly lower than those of Al and Ga, as shown in Figure S11(d). A migration barrier of 0.2 eV for In atoms is again, very low and suggests that In is a mobile element within Li−In intermetallic phases. We also considered lithium (metal) hops to a nearest neighbor vacancy on the metal (lithium) sublattice. Figure S12 of the Supporting Information collects the migration barriers for all symmetrically distinct hops of this type. In Li_2Al, Li_2Ga, and Li_2In, both the lithium and metal prefer to stay on their own sublattice with hops being either unstable or increasing the energy of the crystal. Similar trends are predicted for Li_2Zn, with the exception of one lithium hop to a vacant zinc site, which is predicted to have a very low migration barrier of approximately 35 meV.

Finally, we consider migration barriers within $D0_3$ Li_3M type compounds. This compound is favored by alloying elements Bi, Sb, Sn, In, Zn, and Ag. As an example, Figure 18 shows the Li migration barriers in Li_3Sb. The vacancy in the $D0_3$ form of Li_3M can reside in one of two symmetrically nonequivalent Li sites. A schematic of the Li hop between these two sites is shown in Figure 15b. Figure 18 shows that the Li migration barrier in Li_3Sb is again exceptionally low, being only slightly larger than 0.1 eV. The Li migration barriers in the $D0_3$ forms of Li_3Bi, Li_3Sn, Li_3Ag, Li_3In, and Li_3Zn, as shown in the Supporting Information, are similarly very low, indicating again a very high Li mobility within these compounds provided that there are sufficient vacancies present. In the $D0_3$ crystal structure, lithium is surrounded by both lithium and metal as its nearest neighbors, while the metal only has lithium as nearest neighbors. To quantify the metal mobility in this crystal structure, we consider migration barriers for metal hops to a nearest neighbor vacant site on the lithium sublattice. Ag, Sb, and Bi are predicted to form a rigid metal sublattice in the $D0_3$ structure, with metal nearest neighbor hops being unstable

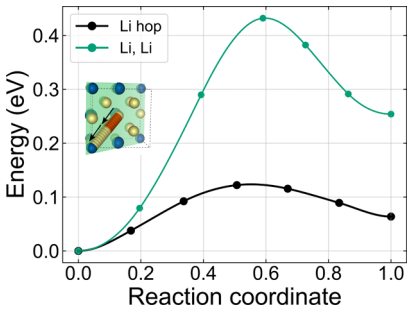

Figure 18. Migration barriers for nearest neighbor lithium hops in $D0_3$ Li_3Sb. The black line shows the migration barrier for a lithium hopping to a nearest neighbor vacant site on the lithium sublattice. The green line shows the migration barrier for a lithium hopping to a nearest neighbor vacant site on the metal sublattice through an unconventional two atom hop as depicted by the schematic in the inset.

or having to overcome high migration barriers as depicted in Figure S7 of the Supporting Information. Conversely, the metals in Li_3Zn, Li_3In, and Li_3Sn favor hops to the lithium sublattice with negligible migration barriers (with the exception of Zn, which has a migration barrier of approximately 350 meV) resulting in a lowering of the total energy of the crystal. This indicates that vacancies prefer to reside on the metal sublattice in these compounds, even if it is at the expense of creating an additional antisite defect on the lithium sublattice. Finally, we also considered migration barriers for lithium hopping to a nearest neighbor vacant site on the metal sublattice. Similar to Li hops in B2 LiAg, nearest neighbor Li hops to the metal sublattice of $D0_3$ are unstable. Instead, lithium can only hop to a vacant site on the metal sublattice through an unconventional two-atom hop mechanism to ensure that the vacant site created by the initial lithium is immediately filled, as shown in the inset of Figure 18. The migration barrier for this hop in Li_3Sb is estimated to be approximately 300 meV, as shown by the green line in Figure 18 which is significantly higher than a simple nearest neighbor lithium hop when restricted to its own sublattice. Figure S7 of the Supporting Information also collects migration barriers for this two-atom hop in Li_3Ag, Li_3Zn, and Li_3Bi.

3.8. Vacancy Formation Energies in Representative Li−M Intermetallic Phases. Vacancies in substitutional alloys are crucial to mediate diffusion. In most metallic alloys and intermetallic compounds, vacancies are entropically stabilized as they generally have a positive formation energy. The vacancy concentration of substitutional alloys are therefore very dilute in most alloys and intermetallics, which often translates into sluggish substitutional diffusion, especially at room temperature. While the calculation of equilibrium vacancy concentrations in disordered solid solutions and intermetallic compounds requires an in depth statistical mechanics treatment,[38,39] it is possible to estimate the vacancy concentrations in well ordered intermetallics upon inspection of grand canonical vacancy formation energies. These can be estimated with DFT calculations using large supercells containing a dilute vacancy as described in Section 2.

Vacancy formation energies were calculated for the intermetallic compounds in the B32, B2, C49, and $D0_3$ structures that are within 10 meV/atom of the convex hull. Grand canonical vacancy formation energies as defined by eq 1 for the different compounds are plotted versus voltage relative

https://doi.org/10.1021/acs.chemmater.4c01279
Chem. Mater. 2024, 36, 7370−7387

to metallic Li in the Supporting Information. In most compounds, the vacancy formation energies are comparable to that of metallic Li, having values that range between 0.4 and 0.6 eV. There are several notable exceptions to this trend that we focus on in more detail.

Figure 19 shows the vacancy formation energies for B32 LiAl. The grand canonical energy to form a vacancy on the Li

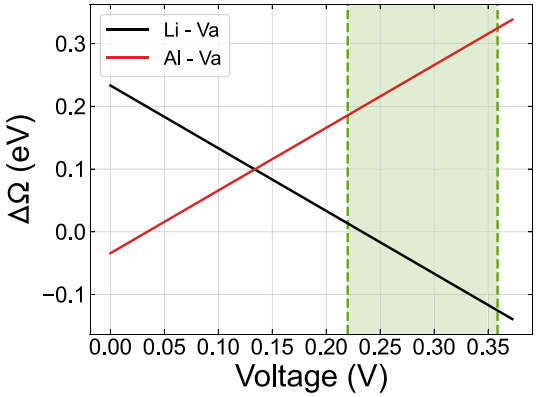

Figure 19. Grand canonical vacancy formation energies in B32 LiAl. The highlighted green section of the plot indicates the voltage window in which the B32 LiAl phase is stable.

sublattice is well below that to form a vacancy on the Al sublattice. The Li vacancy formation energy even becomes negative at higher voltages, indicating that structural vacancies will be present on the Li sublattice at those voltages. This is confirmed by the prediction that supercells of B32 LiAl containing dilute concentrations of vacancies break the convex hull in the Li−Al binary system (Figure S18 of the Supporting Information). The Al vacancy formation energy, while higher than that of a Li vacancy and always positive, is also low when compared to the vacancy formation energy of pure Li in the BCC crystal structure. This suggests that vacancies in the B32 LiAl compound will be more abundant than in metallic Li. In B32 LiGa, a similar trend is predicted, with even more negative vacancy formation energies. Figure S19 in the Supporting Information shows the formation energies of B32 LiGa structures containing dilute concentrations of vacancies. These configurations break the convex hull, having lower formation energies than the perfect B32 LiGa compound. This indicates that the B32 LiAl and LiGa compounds will contain structural vacancies at elevated voltages. In B32 LiZn, both the Li and Zn vacancy formation energies are large, being well above 0.5 eV within the voltage window in which this compound is predicted to be stable. Hence, in contrast to B32 LiAl and B32 LiGa, the LiZn compound will contain a dilute concentration of thermal vacancies.

The B2 LiAg compound is very different from B32 LiAl. In B2 LiAg, vacancies on the Ag sublattice are much more favorable than on the Li sublattice, as shown by the vacancy formation energy in Figure 20. The Li vacancy formation energy in B2 LiAg is especially high, being well above 0.5 eV in the voltage window in which this compound is predicted to be stable. This is consistent with the fact that nearest neighbor hops from the Li sublattice to a vacancy on the Ag sublattice is unstable in B2 LiAg. The cost of placing a vacancy on the Li sublattice and a Li antisite on the Ag sublattice is so high that the end state is not even a local minimum. The low vacancy formation energy on the Ag sublattice combined with relatively

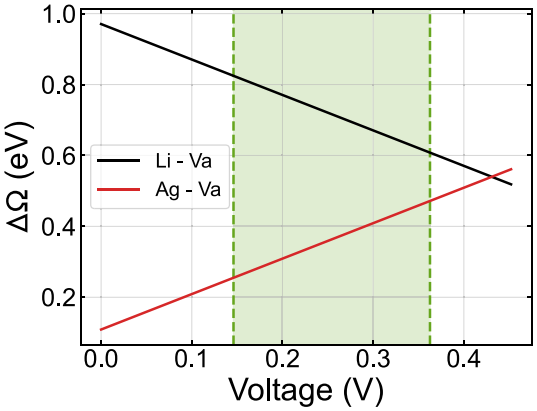

Figure 20. Grand canonical vacancy formation energies in B2 LiAg. The highlighted green section of the plot indicates the voltage window in which the B2 LiAg phase is stable.

low Ag migration barriers suggests that Ag may be the more mobile species in B2 LiAg, although a full kinetic Monte Carlo simulation accounting for all hop mechanisms and the effect of varying degrees of ordering is necessary to rigorously determine the relative mobilities between Li and Ag.[46,47,49]

The C49 Li_2Al, Li_2Ga, and Li_2In compounds are predicted to be stable phases (on the convex hull). The vacancy formation energies in these compounds are all above 0.5 eV in the voltage window in which the compounds are predicted to be stable. They have the highest value in C49 Li_2Al, where they are predicted to be of the order of 0.8 eV. This suggests that these intermetallics will have very dilute equilibrium concentrations of vacancies and therefore lower diffusion coefficients compared to B32.

The Li migration barriers in the $D0_3$ forms of Li_3M with M = Ag, Zn, In, Sn, Sb, and Bi are very low. While the Li vacancy formation energies in Li_3In are quite high, being above that of vacancies on the In sublattice, they are lower in the Ag, Sb, and Bi compounds. In fact, in the Sb and Bi compounds, they even become slightly negative at the higher voltage edge of their stability window. This suggests that Li diffusion in the Ag, Sb, and Bi $D0_3$ compounds should be very rapid. In fact, as described by Chang et al.[94] it may be the origin of voltage hysteresis in the Li−Sb alloy.

4. DISCUSSION

Anode free solid-state batteries promise to enable significant increases in the energy density of Li batteries as they eliminate the need for graphite to store Li at the anode. To be commercially viable, an anode-free battery must be designed to enable the reversible plating and stripping of lithium metal at the anode current collector. Realizing this has proven challenging. Nevertheless, recent studies have shown that certain metals, placed between the solid electrolyte and the current collector, can promote the uniform plating and stripping of Li metal. How these metals affect Li deposition and stripping, however, remains unclear. Undoubtedly, the crystallographic nature of the stable intermetallic phases as well as the atomic diffusion mechanisms and the mechanical properties of those phases play a crucial role. In this study, we have systematically calculated key thermodynamic, kinetic, and mechanical properties of important Li-metal phases, including intermetallic compounds and solid solutions that form when Li is alloyed with Mg, Ag, Zn, Al, Ga, In, Sn, Sb, and Bi.

https://doi.org/10.1021/acs.chemmater.4c01279
Chem. Mater. 2024, 36, 7370−7387

A variety of kinetic models of electrochemical lithium deposition and stripping have been developed.[7,13,95−97] Some models hypothesize that vacancies play a central role and that a sufficient number of vacancies must be available to accommodate the Li^+ ions that emerge from the solid electrolyte during charging of the battery. Vacancy based models that describe stripping during discharge of the battery, hypothesize that vacancies created at the Li metal surface must be able to diffuse away at a sufficiently high rate to prevent a supersaturation of vacancies that can then coalesce to form voids. Void formation is undesirable as it can result in lithium metal island formation and loss of contact with the current collector.

Our DFT calculations predict that vacancies are exceptionally mobile in metallic Li and in many of the Li intermetallic compounds and solid solutions. The migration barriers of Li and Mg in the BCC Li−Mg solid solution, for example, is remarkably low, having values that deviate negligibly from an average of 75 meV. Vacancies within this alloy, therefore, have very high mobilities, as confirmed with kinetic Monte Carlo simulations, which predict a very high vacancy tracer diffusion coefficient in the Li−Mg alloy. Similar low migration barriers are predicted in a large number of the intermetallic compounds investigated in this work. The B32 LiM, C49 Li_2M, and $D0_3$ Li_3M intermetallic crystal structures contain local environments that are representative of many other Li-M intermetallic compounds with different stoichiometries. These intermetallic crystal structures were therefore studied as model systems to establish trends in Li and metal mobilities. The calculated migration barriers for Li hops along the Li sublattices in most B32 LiM, C49 Li_2M, and $D0_3$ Li_3M compounds are very low, with values ranging between 100 and 200 meV. These migration barriers rival those of the fastest solid-state superion conductors.[85−90] The migration barriers of the metal alloying elements in the same compounds, in contrast, are with few exceptions predicted to be significantly higher than the Li migration barriers. This suggests that Li is generally more mobile than the metallic alloying element within most Li-M intermetallics. We also discovered a variety of unusual diffusion mechanisms when Li migrates from its own sublattice to the metal sublattice of the intermetallic compound. In the B2 LiAg and the $D0_3$ Li_3Ag, Li_3Sb, and Li_3Bi compounds, elementary nearest neighbor Li hops to the vacancies on the metal sublattice are predicted to be unstable. Instead, hop events involving two atoms at a time are predicted to be necessary to enable Li migration to the metal sublattice. This is similar to diffusion mechanisms in the B2 NiAl intermetallic compound.[47,60,93]

Diffusion in substitutional solids and intermetallic compounds is generally mediated by vacancies.[46,48,49] In most substitutional solids, the concentration of vacancies is very low. In fact, DFT calculations predict a vacancy formation energy of 0.5 eV in BCC Li, a high value that translates into a low equilibrium vacancy concentration. The vacancy formation energy remains high upon alloying with Mg to form the BCC Li−Mg solid solution. Our calculations also predict that the formation energies are high in most Li-M intermetallic compounds studied in this work. Since vacancies mediate diffusion, a low vacancy concentration results in low diffusion coefficients,[46,48,49,63] in spite of the exceptionally rapid hop kinetics once a vacancy is present. There are several notable exceptions to this trend, however. Both the LiAl and LiGa intermetallic compounds, which adopt the B32 zintl crystal structure, favor structural vacancies on their Li sublattices. As described in Section 3.5, the thermodynamic stability of a vacancy concentration of approximately 5% on the Li sublattices (2.5% in total) of LiAl and LiGa arises from their unique electronic structure. The metal atoms of both compounds have a diamond sublattice similar to Si, but due to the presence of Li, are semimetals with a partial overlap of their bonding valence band and their antibonding conduction band. To avoid filling antibonding states, there is a drive to lower the Fermi levels of the compounds, which can be realized through the removal of a small fraction of Li and as a result the stabilization of structural vacancies. Because structural vacancies are thermodynamically stable in the B32 LiAl and LiGa compounds and their Li migration barriers are very low, these compounds form a class of intermetallic compounds that enable exceptionally fast Li transport. For similar reasons, the $D0_3$ Li_3Sb and Li_3Bi intermetallic compounds also enable fast Li diffusion. There are several battery architectures, such as the one proposed by Liang et al.,[98] where a lithium foil coated with a film of lithium intermetallic compound at the anode is shown to prevent dendritic growth upon plating/stripping. In these architectures, it is desirable to have compounds that enable very fast Li diffusion. Intermetallic compounds such as B32 LiAl, B32 LiGa, $D0_3$ Li_3Sb, and $D0_3$ Li_3Bi might be suitable candidates for such scenarios.

Several kinetic models of Li plating and stripping account for the role of plastic and creep deformation of metallic Li.[28,99−103] Past DFT calculations[50,51] and those presented in this study predict that Li has a highly unusual zero kelvin energy landscape, with the BCC, FCC, HCP, and all other stackings of close-packed layers having energies that are essentially identical to each other within the numerical precision of DFT calculations. Furthermore, the barriers along pathways that connect BCC to a close-packed crystal structure is negligible.[51] While these predictions do not account for vibrational entropy, they pose fundamental questions about the true nature and local structure of BCC Li at room temperature. Is the room temperature form of Li truly a BCC structure, entropically stabilized by anharmonic vibrational excitations[56,57] or is it a collection of nanodomains of close-packed stackings that can be derived from a common parent BCC structure and therefore generate a BCC diffraction pattern? If it *is* a collection of nanodomains of close-packed stackings which can be derived from the common BCC parent crystal structure through local strains, defects such as stacking faults, or twin boundaries, it might result in broadening of peaks in diffraction patterns.[104] The true nature of BCC Li will have important consequences for its plastic and creep deformation mechanisms. Furthermore, the high degree of anharmonicity in the zero-kelvin Li energy surfaces will have implications for the types of grain boundary structures that are favored at room temperature and how these grain boundaries can generate vacancies for bulk diffusion.[105] The equilibrium and dynamical nature of the room temperature form of metallic Li can be resolved with large-scale Monte Carlo or molecular dynamics simulations applied to an energy model of Li that accurately reproduces the very anharmonic landscape revealed by DFT calculations presented in this work and in past studies.[50,51] DFT calculations in this work show that alloying additions to BCC Li do affect the energy surface along the Bain and Burgers paths, but compounds that are Li-rich maintain a high degree of anharmonicity.

https://doi.org/10.1021/acs.chemmater.4c01279
Chem. Mater. 2024, 36, 7370−7387

5. CONCLUSION

First-principles density functional theory calculations of metallic lithium and its alloys predict a variety of properties that are unusual for metals. The energy of lithium as a function of strain and shuffle order parameters is highly anharmonic, exhibiting negligible barriers along structural pathways that connect BCC to FCC and HCP. While this unusual anharmonicity persists in alloys that are Li-rich, an increase in the concentration of alloying elements leads to a stiffening of the BCC crystal structure. Lithium and almost all Li-metal intermetallic compounds studied in this work have exceptionally low migration barriers for diffusion. The migration barriers rival those of the fastest solid electrolytes. The migration barriers for metal diffusion in most Li-metal intermetallics, in contrast, are much higher. Vacancies, which are crucial in mediating diffusion in substitutional alloys and intermetallic compounds, are predicted to be present in very low concentrations, being thermally generated due to entropic driving forces. Most Li-metal compounds have high vacancy formation energies, which translates into low diffusion coefficients. However, once vacancies are formed, they are exceptionally mobile due to the low migration barriers for diffusion. A small subset of intermetallics, such as B32 LiAl and LiGa, favor structural vacancies at compositions of 1−2.5%. These compounds should exhibit very rapid diffusion.

■ ASSOCIATED CONTENT

Data Availability Statement

All the data will be made available through Materials Commons.

Supporting Information

The Supporting Information is available free of charge at https://pubs.acs.org/doi/10.1021/acs.chemmater.4c01279.

DFT global convex hulls and voltage curves for Li with Mg, Ca, Ag, Zn, Al, Ga, In, Sn, Sb, and Bi; nudged elastic band calculations for lithium-vacancy and metal-vacancy hops, grand canonical vacancy formation energies as a function of voltage for various lithium intermetallics in B32, $D0_3$, C49, and B2 crystal structures; crystal orbital Hamiltonian population (COHP) analysis for B32 LiAl, LiAl without Li, LiSb, and diamond cubic Si; volume per metal atom for various intermetallic structures; Li−Al, Li−Ga, and Li−Zn DFT convex hulls (PDF)

■ AUTHOR INFORMATION

Corresponding Author

Anton Van der Ven − *Materials Department, University of California Santa Barbara, Santa Barbara, California 93106, United States*; Email: avdv@ucsb.edu

Authors

Sesha Sai Behara − *Materials Department, University of California Santa Barbara, Santa Barbara, California 93106, United States*; orcid.org/0000-0003-2144-4586

Jeremiah Thomas − *Materials Department, University of California Santa Barbara, Santa Barbara, California 93106, United States*; orcid.org/0009-0009-4011-4102

Complete contact information is available at: https://pubs.acs.org/10.1021/acs.chemmater.4c01279

Notes

The authors declare no competing financial interest.

■ ACKNOWLEDGMENTS

We are grateful for insightful discussions with Drs. Joseph Shiang, Krishna Garikipati, and Vishnu Sundaresan. S.S.B. thanks Jonathan Li and Derick E. Ober for insightful discussions. S.S.B. and A.V.d.V. were supported by the Defense Advanced Research Projects Agency under Contract HR001122C0097. J.T. is supported by the NSF under Contract 2311370. Use was made of computational facilities purchased with funds from the National Science Foundation (Grant CNS-1725797) and administered by the Center for Scientific Computing (CSC). The CSC is supported by the California NanoSystems Institute and the Materials Research Science and Engineering Center (MRSEC; NSF DMR 2308708) at UC Santa Barbara. We are also grateful for the resources of the National Energy Research Scientific Computing Center (NERSC), a U.S. Department of Energy Office of Science User Facility located at Lawrence Berkeley National Laboratory, operated under Contract DE-AC02-05CH11231 using NERSC Award BES-ERCAP0026626. Research was also carried out at the Center for Functional Nanomaterials, Brookhaven National Laboratory, through the U.S. Department of Energy, Office of Basic Energy Sciences, Contract DE-AC02-98CH10866, under Award CFN312109.

■ REFERENCES

(1) Wang, M. J.; Kazyak, E.; Dasgupta, N. P.; Sakamoto, J. Transitioning solid-state batteries from lab to market: Linking electro-chemo-mechanics with practical considerations. *Joule* **2021**, *5*, 1371−1390.

(2) Porz, L.; Swamy, T.; Sheldon, B. W.; Rettenwander, D.; Frömling, T.; Thaman, H. L.; Berendts, S.; Uecker, R.; Carter, W. C.; Chiang, Y.-M. Mechanism of lithium metal penetration through inorganic solid electrolytes. *Adv. Energy Mater.* **2017**, *7*, 1701003.

(3) Kasemchainan, J.; Zekoll, S.; Spencer Jolly, D.; Ning, Z.; Hartley, G. O.; Marrow, J.; Bruce, P. G. Critical stripping current leads to dendrite formation on plating in lithium anode solid electrolyte cells. *Nature materials* **2019**, *18*, 1105−1111.

(4) Kim, S.; Jung, C.; Kim, H.; Thomas-Alyea, K. E.; Yoon, G.; Kim, B.; Badding, M. E.; Song, Z.; Chang, J.; Kim, J.; et al. The role of interlayer chemistry in Li-metal growth through a garnet-type solid electrolyte. *Adv. Energy Mater.* **2020**, *10*, 1903993.

(5) Ning, Z.; Jolly, D. S.; Li, G.; De Meyere, R.; Pu, S. D.; Chen, Y.; Kasemchainan, J.; Ihli, J.; Gong, C.; Liu, B.; et al. Visualizing plating-induced cracking in lithium-anode solid-electrolyte cells. *Nature materials* **2021**, *20*, 1121−1129.

(6) Kazyak, E.; Wang, M. J.; Lee, K.; Yadavalli, S.; Sanchez, A. J.; Thouless, M.; Sakamoto, J.; Dasgupta, N. P. Understanding the electro-chemo-mechanics of Li plating in anode-free solid-state batteries with operando 3D microscopy. *Matter* **2022**, *5*, 3912−3934.

(7) Krauskopf, T.; Richter, F. H.; Zeier, W. G.; Janek, J. Physicochemical concepts of the lithium metal anode in solid-state batteries. *Chem. Rev.* **2020**, *120*, 7745−7794.

(8) Krauskopf, T.; Dippel, R.; Hartmann, H.; Peppler, K.; Mogwitz, B.; Richter, F. H.; Zeier, W. G.; Janek, J. Lithium-metal growth kinetics on LLZO garnet-type solid electrolytes. *Joule* **2019**, *3*, 2030−2049.

(9) Kazyak, E.; Garcia-Mendez, R.; LePage, W. S.; Sharafi, A.; Davis, A. L.; Sanchez, A. J.; Chen, K.-H.; Haslam, C.; Sakamoto, J.; Dasgupta, N. P. Li penetration in ceramic solid electrolytes: operando microscopy analysis of morphology, propagation, and reversibility. *Matter* **2020**, *2*, 1025−1048.

(10) Tsai, C.-L.; Roddatis, V.; Chandran, C. V.; Ma, Q.; Uhlenbruck, S.; Bram, M.; Heitjans, P.; Guillon, O. Li7La3Zr2O12 interface modification for Li dendrite prevention. *ACS Appl. Mater. Interfaces* **2016**, *8*, 10617−10626.

(11) He, M.; Cui, Z.; Chen, C.; Li, Y.; Guo, X. Formation of self-limited, stable and conductive interfaces between garnet electrolytes and lithium anodes for reversible lithium cycling in solid-state batteries. *Journal of Materials Chemistry A* **2018**, *6*, 11463−11470.
(12) Feng, W.; Dong, X.; Li, P.; Wang, Y.; Xia, Y. Interfacial modification of Li/Garnet electrolyte by a lithiophilic and breathing interlayer. *J. Power Sources* **2019**, *419*, 91−98.
(13) Krauskopf, T.; Mogwitz, B.; Rosenbach, C.; Zeier, W. G.; Janek, J. Diffusion limitation of lithium metal and Li−Mg alloy anodes on LLZO type solid electrolytes as a function of temperature and pressure. *Adv. Energy Mater.* **2019**, *9*, 1902568.
(14) Yang, C.; Xie, H.; Ping, W.; Fu, K.; Liu, B.; Rao, J.; Dai, J.; Wang, C.; Pastel, G.; Hu, L. An electron/ion dual-conductive alloy framework for high-rate and high-capacity solid-state lithium-metal batteries. *Adv. Mater.* **2019**, *31*, 1804815.
(15) Lee, Y.-G.; Fujiki, S.; Jung, C.; Suzuki, N.; Yashiro, N.; Omoda, R.; Ko, D.-S.; Shiratsuchi, T.; Sugimoto, T.; Ryu, S.; et al. High-energy long-cycling all-solid-state lithium metal batteries enabled by silver−carbon composite anodes. *Nature Energy* **2020**, *5*, 299−308.
(16) Zhong, Y.; Xie, Y.; Hwang, S.; Wang, Q.; Cha, J. J.; Su, D.; Wang, H. A highly efficient all-solid-state lithium/electrolyte interface induced by an energetic reaction. *Angew. Chem., Int. Ed.* **2020**, *59*, 14003−14008.
(17) Lee, K.; Han, S.; Lee, J.; Lee, S.; Kim, J.; Ko, Y.; Kim, S.; Yoon, K.; Song, J.-H.; Noh, J. H.; et al. Multifunctional interface for high-rate and long-durable garnet-type solid electrolyte in lithium metal batteries. *ACS Energy Lett.* **2022**, *7*, 381−389.
(18) He, X.; Ji, X.; Zhang, B.; Rodrigo, N. D.; Hou, S.; Gaskell, K.; Deng, T.; Wan, H.; Liu, S.; Xu, J.; et al. Tuning interface lithiophobicity for lithium metal solid-state batteries. *ACS Energy Lett.* **2022**, *7*, 131−139.
(19) Lee, S.; Lee, K.-s.; Kim, S.; Yoon, K.; Han, S.; Lee, M. H.; Ko, Y.; Noh, J. H.; Kim, W.; Kang, K. Design of a lithiophilic and electron-blocking interlayer for dendrite-free lithium-metal solid-state batteries. *Sci. Adv.* **2022**, *8*, No. eabq0153.
(20) Sandoval, S. E.; Lewis, J. A.; Vishnugopi, B. S.; Nelson, D. L.; Schneider, M. M.; Cortes, F. J. Q.; Matthews, C. M.; Watt, J.; Tian, M.; Shevchenko, P.; et al. Structural and electrochemical evolution of alloy interfacial layers in anode-free solid-state batteries. *Joule* **2023**, *7*, 2054−2073.
(21) Kim, J.-S.; Yoon, G.; Kim, S.; Sugata, S.; Yashiro, N.; Suzuki, S.; Lee, M.-J.; Kim, R.; Badding, M.; Song, Z.; et al. Surface engineering of inorganic solid-state electrolytes via interlayers strategy for developing long-cycling quasi-all-solid-state lithium batteries. *Nat. Commun.* **2023**, *14*, 782.
(22) Fu, K.; Gong, Y.; Liu, B.; Zhu, Y.; Xu, S.; Yao, Y.; Luo, W.; Wang, C.; Lacey, S. D.; Dai, J.; et al. Toward garnet electrolyte-based Li metal batteries: An ultrathin, highly effective, artificial solid-state electrolyte/metallic Li interface. *Sci. Adv.* **2017**, *3*, No. e1601659.
(23) Fu, K.; Gong, Y.; Fu, Z.; Xie, H.; Yao, Y.; Liu, B.; Carter, M.; Wachsman, E.; Hu, L. Transient behavior of the metal interface in lithium metal−garnet batteries. *Angew. Chem., Int. Ed.* **2017**, *56*, 14942−14947.
(24) Cai, M.; Lu, Y.; Su, J.; Ruan, Y.; Chen, C.; Chowdari, B. V.; Wen, Z. In situ lithiophilic layer from H+/Li+ exchange on garnet surface for the stable lithium-solid electrolyte interface. *ACS Appl. Mater. Interfaces* **2019**, *11*, 35030−35038.
(25) Jin, S.; Ye, Y.; Niu, Y.; Xu, Y.; Jin, H.; Wang, J.; Sun, Z.; Cao, A.; Wu, X.; Luo, Y.; et al. Solid−solution-based metal alloy phase for highly reversible lithium metal anode. *J. Am. Chem. Soc.* **2020**, *142*, 8818−8826.
(26) Choi, S. H.; Lee, S. J.; Yoo, D.-J.; Park, J. H.; Park, J.-H.; Ko, Y. N.; Park, J.; Sung, Y.-E.; Chung, S.-Y.; Kim, H.; Choi, J. W. Marginal magnesium doping for high-performance lithium metal batteries. *Adv. Energy Mater.* **2019**, *9*, 1902278.
(27) Yan, K.; Lu, Z.; Lee, H.-W.; Xiong, F.; Hsu, P.-C.; Li, Y.; Zhao, J.; Chu, S.; Cui, Y. Selective deposition and stable encapsulation of lithium through heterogeneous seeded growth. *Nat. Energy* **2016**, *1*, 1−8.
(28) Kim, S. Y.; Li, J. Porous mixed ionic electronic conductor interlayers for solid-state batteries. *Energy Mater. Adv.* **2021**, *2021*, 1519569.
(29) Perdew, J. P.; Burke, K.; Ernzerhof, M. Generalized gradient approximation made simple. *Physical review letters* **1996**, *77*, 3865.
(30) Kresse, G.; Hafner, J. Ab initio molecular dynamics for liquid metals. *Phys. Rev. B* **1993**, *47*, 558.
(31) Kresse, G.; Furthmüller, J. Efficiency of ab-initio total energy calculations for metals and semiconductors using a plane-wave basis set. *Computational materials science* **1996**, *6*, 15−50.
(32) Kresse, G.; Furthmüller, J. Efficient iterative schemes for ab initio total-energy calculations using a plane-wave basis set. *Phys. Rev. B* **1996**, *54*, 11169.
(33) Blöchl, P. E. Projector augmented-wave method. *Phys. Rev. B* **1994**, *50*, 17953.
(34) Henkelman, G.; Uberuaga, B. P.; Jónsson, H. A climbing image nudged elastic band method for finding saddle points and minimum energy paths. *J. Chem. Phys.* **2000**, *113*, 9901−9904.
(35) Henkelman, G.; Jónsson, H. Improved tangent estimate in the nudged elastic band method for finding minimum energy paths and saddle points. *J. Chem. Phys.* **2000**, *113*, 9978−9985.
(36) Sheppard, D.; Terrell, R.; Henkelman, G. Optimization methods for finding minimum energy paths. *J. Chem. Phys.* **2008**, *128*, 134106.
(37) Puchala, B.; Thomas, J. C.; Natarajan, A. R.; Goiri, J. G.; Behara, S. S.; Kaufman, J. L.; Van der Ven, A. CASM—A software package for first-principles based study of multicomponent crystalline solids. *Comput. Mater. Sci.* **2023**, *217*, 111897.
(38) Van der Ven, A.; Ceder, G. Vacancies in ordered and disordered binary alloys treated with the cluster expansion. *Phys. Rev. B* **2005**, *71*, 054102.
(39) Belak, A. A.; Van der Ven, A. Effect of disorder on the dilute equilibrium vacancy concentrations of multicomponent crystalline solids. *Phys. Rev. B* **2015**, *91*, 224109.
(40) Van der Ven, A.; Deng, Z.; Banerjee, S.; Ong, S. P. Rechargeable alkali-ion battery materials: theory and computation. *Chem. Rev.* **2020**, *120*, 6977−7019.
(41) Sanchez, J. M.; Ducastelle, F.; Gratias, D. Generalized cluster description of multicomponent systems. *Physica A: Statistical Mechanics and its Applications* **1984**, *128*, 334−350.
(42) De Fontaine, D. *Solid State Physics*; Elsevier, 1994; Vol. *47*; pp 33−176.
(43) Puchala, B.; Thomas, J. C.; der Ven, A. V. CASM Monte Carlo: Calculations of the thermodynamic and kinetic properties of complex multicomponent crystals. *arXiv* **2023**, 2309.11761 (https://arxiv.org/abs/2309.11761). Accessed Jul 10, 2024.
(44) Van der Ven, A.; Thomas, J. C.; Puchala, B.; Natarajan, A. R. First-principles statistical mechanics of multicomponent crystals. *Annu. Rev. Mater. Res.* **2018**, *48*, 27−55.
(45) Ober, D. E.; der Ven, A. V. Thermodynamically Informed Priors for Uncertainty Propagation in First-Principles Statistical Mechanics. *arXiv* **2023**, 2309.12255 (https://arxiv.org/abs/2309.12255). Accessed Jul 10, 2024.
(46) Van der Ven, A.; Ceder, G. First principles calculation of the interdiffusion coefficient in binary alloys. *Physical review letters* **2005**, *94*, 045901.
(47) Xu, Q.; Van der Ven, A. Atomic transport in ordered compounds mediated by local disorder: Diffusion in B 2-Ni x Al 1- x. *Phys. Rev. B* **2010**, *81*, 064303.
(48) Van der Ven, A.; Yu, H.-C.; Ceder, G.; Thornton, K. Vacancy mediated substitutional diffusion in binary crystalline solids. *Prog. Mater. Sci.* **2010**, *55*, 61−105.
(49) Goiri, J. G.; Kolli, S. K.; Van der Ven, A. Role of short-and long-range ordering on diffusion in Ni-Al alloys. *Phys. Rev. Mater.* **2019**, *3*, 093402.
(50) Ackland, G. J.; Dunuwille, M.; Martinez-Canales, M.; Loa, I.; Zhang, R.; Sinogeikin, S.; Cai, W.; Deemyad, S. Quantum and isotope effects in lithium metal. *Science* **2017**, *356*, 1254−1259.

https://doi.org/10.1021/acs.chemmater.4c01279
Chem. Mater. 2024, 36, 7370−7387

(51) Raju Natarajan, A.; Van der Ven, A. Toward an understanding of deformation mechanisms in metallic lithium and sodium from first-principles. *Chem. Mater.* **2019**, *31*, 8222−8229.
(52) Berliner, R.; Fajen, O.; Smith, H.; Hitterman, R. Neutron powder-diffraction studies of lithium, sodium, and potassium metal. *Phys. Rev. B* **1989**, *40*, 12086.
(53) Smith, H.; Berliner, R.; Jorgensen, J. Martensitic transformation from BCC to 9R and FCC in metallic lithium. *Physica B: Condensed Matter* **1989**, *156*, 53−55.
(54) Smith, H.; Berliner, R.; Jorgensen, J.; Nielsen, M.; Trivisonno, J. Pressure effects on the martensitic transformation in metallic lithium. *Phys. Rev. B* **1990**, *41*, 1231.
(55) Thomas, J. C.; Van der Ven, A. The exploration of nonlinear elasticity and its efficient parameterization for crystalline materials. *Journal of the Mechanics and Physics of Solids* **2017**, *107*, 76−95.
(56) Hutcheon, M.; Needs, R. Structural and vibrational properties of lithium under ambient conditions within density functional theory. *Phys. Rev. B* **2019**, *99*, 014111.
(57) Jerabek, P.; Burrows, A.; Schwerdtfeger, P. Solving a problem with a single parameter: a smooth bcc to fcc phase transition for metallic lithium. *Chem. Commun.* **2022**, *58*, 13369−13372.
(58) Frank, W.; Breier, U.; Elsässer, C.; Fähnle, M. First-principles calculations of absolute concentrations and self-diffusion constants of vacancies in lithium. *Physical review letters* **1996**, *77*, 518.
(59) Schott, V.; Fähnle, M.; Madden, P. Theory of self-diffusion in alkali metals: I. Results for monovacancies in Li, Na, and K. *J. Phys.: Condens. Matter* **2000**, *12*, 1171.
(60) Xu, Q.; Van der Ven, A. First-principles investigation of migration barriers and point defect complexes in B2−NiAl. *Intermetallics* **2009**, *17*, 319−329.
(61) Mantina, M.; Wang, Y.; Chen, L.; Liu, Z.; Wolverton, C. First principles impurity diffusion coefficients. *Acta Mater.* **2009**, *57*, 4102−4108.
(62) Wu, H.; Mayeshiba, T.; Morgan, D. High-throughput ab-initio dilute solute diffusion database. *Sci. Data* **2016**, *3*, 1−11.
(63) Balluffi, R. W.; Allen, S. M.; Carter, W. C. *Kinetics of Materials*; John Wiley & Sons, 2005.
(64) Kadkhodaei, S.; van de Walle, A. A simple local expression for the prefactor in transition state theory. *J. Chem. Phys.* **2019**, *150*, 144105.
(65) Lodding, A.; Mundy, J.; Ott, A. Isotope inter-diffusion and self-diffusion in solid lithium metal. *physica status solidi (b)* **1970**, *38*, 559−569.
(66) Siniscalchi, M.; Liu, J.; Gibson, J. S.; Turrell, S. J.; Aspinall, J.; Weatherup, R. S.; Pasta, M.; Speller, S. C.; Grovenor, C. R. On the relative importance of Li bulk diffusivity and interface morphology in determining the stripped capacity of metallic anodes in solid-state batteries. *ACS Energy Lett.* **2022**, *7*, 3593−3599.
(67) Nayeb-Hashemi, A.; Clark, J. B.; Pelton, A. The Li-Mg (lithium-magnesium) system. *Bulletin of Alloy Phase Diagrams* **1984**, *5*, 365−374.
(68) Goiri, J. G.; Van der Ven, A. Phase and structural stability in Ni-Al systems from first principles. *Phys. Rev. B* **2016**, *94*, 094111.
(69) Van der Ven, A.; Ceder, G.; Asta, M.; Tepesch, P. First-principles theory of ionic diffusion with nondilute carriers. *Phys. Rev. B* **2001**, *64*, 184307.
(70) Van der Ven, A.; Thomas, J. C.; Xu, Q.; Swoboda, B.; Morgan, D. Nondilute diffusion from first principles: Li diffusion in Li x TiS 2. *Phys. Rev. B* **2008**, *78*, 104306.
(71) Bhattacharya, J.; Van der Ven, A. First-principles study of competing mechanisms of nondilute Li diffusion in spinel Li x TiS 2. *Phys. Rev. B* **2011**, *83*, 144302.
(72) Fattahpour, S.; Davariashtiyani, A.; Kadkhodaei, S. Understanding the role of anharmonic phonons in diffusion of bcc metals. *Phys. Rev. Mater.* **2022**, *6*, 023803.
(73) Behara, S. S.; Van der Ven, A. Role of short-range order on diffusion coefficients in Li-Mg alloy. To be submitted 2024.
(74) Kolli, S. K.; Natarajan, A. R.; Thomas, J. C.; Pollock, T. M.; Van der Ven, A. Discovering hierarchies among intermetallic crystal structures. *Phys. Rev. Mater.* **2020**, *4*, 113604.
(75) De Fontaine, D.; Ceder, G.; Asta, M. Low-temperature long-range oxygen order in YBa2Cu3O z. *Nature* **1990**, *343*, 544−546.
(76) Natarajan, A. R.; Solomon, E. L.; Puchala, B.; Marquis, E. A.; Van der Ven, A. On the early stages of precipitation in dilute Mg−Nd alloys. *Acta Mater.* **2016**, *108*, 367−379.
(77) Natarajan, A. R.; Van der Ven, A. A unified description of ordering in HCP Mg-RE alloys. *Acta Mater.* **2017**, *124*, 620−632.
(78) Kaufman, J. L.; Vinckevičiūtė, J.; Krishna Kolli, S.; Gabriel Goiri, J.; Van der Ven, A. Understanding intercalation compounds for sodium-ion batteries and beyond. *Philos. Trans. R. Soc., A* **2019**, *377*, 20190020.
(79) Kaufman, J. L.; Van der Ven, A. Na x CoO 2 phase stability and hierarchical orderings in the O3/P3 structure family. *Phys. Rev. Mater.* **2019**, *3*, 015402.
(80) Kaufman, J. L.; Van der Ven, A. Cation diffusion facilitated by antiphase boundaries in layered intercalation compounds. *Chem. Mater.* **2022**, *34*, 1889−1896.
(81) Jain, A.; Hautier, G.; Ong, S. P.; Moore, C. J.; Fischer, C. C.; Persson, K. A.; Ceder, G. Formation enthalpies by mixing GGA and GGA+ U calculations. *Phys. Rev. B* **2011**, *84*, 045115.
(82) Zunger, A. First-principles theoretical study on the electronic properties of the B 32 intermetallic compound LiAl. *Phys. Rev. B* **1978**, *17*, 2582.
(83) Asada, T.; Jarlborg, T.; Freeman, A. J. Self-consistent electronic structure of the intermetallic compound LiA1. *Phys. Rev. B* **1981**, *24*, 510.
(84) Kishio, K.; Brittain, J. Defect structure of β-LiAl. *J. Phys. Chem. Solids* **1979**, *40*, 933−940.
(85) Kamaya, N.; Homma, K.; Yamakawa, Y.; Hirayama, M.; Kanno, R.; Yonemura, M.; Kamiyama, T.; Kato, Y.; Hama, S.; Kawamoto, K.; et al. A lithium superionic conductor. *Nature materials* **2011**, *10*, 682−686.
(86) Emly, A.; Kioupakis, E.; Van der Ven, A. Phase stability and transport mechanisms in antiperovskite Li3OCl and Li3OBr superionic conductors. *Chem. Mater.* **2013**, *25*, 4663−4670.
(87) Wang, Y.; Richards, W. D.; Ong, S. P.; Miara, L. J.; Kim, J. C.; Mo, Y.; Ceder, G. Design principles for solid-state lithium superionic conductors. *Nature materials* **2015**, *14*, 1026−1031.
(88) He, X.; Zhu, Y.; Mo, Y. Origin of fast ion diffusion in super-ionic conductors. *Nat. Commun.* **2017**, *8*, 15893.
(89) Uitz, M.; Epp, V.; Bottke, P.; Wilkening, M. Ion dynamics in solid electrolytes for lithium batteries: Probing jump rates and activation energies through time-domain Li NMR. *Journal of Electroceramics* **2017**, *38*, 142−156.
(90) Di Stefano, D.; Miglio, A.; Robeyns, K.; Filinchuk, Y.; Lechartier, M.; Senyshyn, A.; Ishida, H.; Spannenberger, S.; Prutsch, D.; Lunghammer, S.; et al. Superionic diffusion through frustrated energy landscape. *Chem.* **2019**, *5*, 2450−2460.
(91) Wang, J.; He, T.; Yang, X.; Cai, Z.; Wang, Y.; Lacivita, V.; Kim, H.; Ouyang, B.; Ceder, G. Design principles for NASICON super-ionic conductors. *Nat. Commun.* **2023**, *14*, 5210.
(92) Jun, K.; Sun, Y.; Xiao, Y.; Zeng, Y.; Kim, R.; Kim, H.; Miara, L. J.; Im, D.; Wang, Y.; Ceder, G. Lithium superionic conductors with corner-sharing frameworks. *Nature materials* **2022**, *21*, 924−931.
(93) Mishin, Y.; Lozovoi, A.; Alavi, A. Evaluation of diffusion mechanisms in NiAl by embedded-atom and first-principles calculations. *Phys. Rev. B* **2003**, *67*, 014201.
(94) Chang, D.; Huo, H.; Johnston, K. E.; Ménétrier, M.; Monconduit, L.; Grey, C. P.; Van der Ven, A. Elucidating the origins of phase transformation hysteresis during electrochemical cycling of Li−Sb electrodes. *Journal of Materials Chemistry A* **2015**, *3*, 18928−18943.
(95) Krauskopf, T.; Hartmann, H.; Zeier, W. G.; Janek, J. Toward a fundamental understanding of the lithium metal anode in solid-state batteries—an electrochemo-mechanical study on the garnet-type solid

electrolyte Li6. 25Al0. 25La3Zr2O12. *ACS Appl. Mater. Interfaces* **2019**, *11*, 14463−14477.
(96) Shishvan, S. S.; Fleck, N. A.; McMeeking, R. M.; Deshpande, V. S. Vacancy diffusion and its consequences for void growth at the interface of a stripping metal electrode and solid electrolyte. *Electrochimica acta* **2023**, *467*, 143081.
(97) Shishvan, S.; Fleck, N.; McMeeking, R.; Deshpande, V. Void growth in metal anodes in solid-state batteries: Recent progress and gaps in understanding. *European Journal of Mechanics-A/Solids* **2023**, *100*, 104998.
(98) Liang, X.; Pang, Q.; Kochetkov, I. R.; Sempere, M. S.; Huang, H.; Sun, X.; Nazar, L. F. A facile surface chemistry route to a stabilized lithium metal anode. *Nat. Energy* **2017**, *2*, 1−7.
(99) LePage, W. S.; Chen, Y.; Kazyak, E.; Chen, K.-H.; Sanchez, A. J.; Poli, A.; Arruda, E. M.; Thouless, M.; Dasgupta, N. P. Lithium mechanics: roles of strain rate and temperature and implications for lithium metal batteries. *J. Electrochem. Soc.* **2019**, *166*, A89−A97.
(100) Chen, Y.; Wang, Z.; Li, X.; Yao, X.; Wang, C.; Li, Y.; Xue, W.; Yu, D.; Kim, S. Y.; Yang, F.; et al. Li metal deposition and stripping in a solid-state battery via Coble creep. *Nature* **2020**, *578*, 251−255.
(101) Wang, Z.; Li, X.; Chen, Y.; Pei, K.; Mai, Y.-W.; Zhang, S.; Li, J. Creep-enabled 3D solid-state lithium-metal battery. *Chem* **2020**, *6*, 2878−2892.
(102) Fincher, C. D.; Ojeda, D.; Zhang, Y.; Pharr, G. M.; Pharr, M. Mechanical properties of metallic lithium: from nano to bulk scales. *Acta Mater.* **2020**, *186*, 215−222.
(103) Jun, D.; Park, S. H.; Jung, J. E.; Lee, S. G.; Kim, K. S.; Kim, J. Y.; Bae, K. Y.; Son, S.; Lee, Y. J. Ultra-Stable Breathing Anode for Li-Free All-Solid-State Battery Based on Li Concentration Gradient in Magnesium Particles. *Adv. Funct. Mater.* **2024**, *34*, 2310259.
(104) Berliner, R.; Werner, S. Effect of stacking faults on diffraction: The structure of lithium metal. *Phys. Rev. B* **1986**, *34*, 3586.
(105) Yu, H.-C.; Van der Ven, A.; Thornton, K. Theory of grain boundary diffusion induced by the Kirkendall effect. *Appl. Phys. Lett.* **2008**, *93*, 091908.

https://doi.org/10.1021/acs.chemmater.4c01279
Chem. Mater. 2024, 36, 7370−7387